~~Comparing~~Comparison of scattering ratio ~~products~~profiles retrieved from ALADIN/Aeolus and CALIOP/CALIPSO observations~~: sensitivity, comparability,~~ and ~~temporal evolution~~preliminary estimates of cloud fraction profiles

Artem G. Feofilov[1], Hélène Chepfer[1], Vincent ~~Noel~~[2]Noël[2], Rodrigo Guzman[1], Cyprien Gindre[1], Po-Lun Ma[3], and Marjolaine ~~Chiriaco~~[3]Chiriaco[4]

[1]~~LMD~~[1] LMD/IPSL, Sorbonne Université, UPMC Univ Paris 06, CNRS, École ~~polytechnique, Palaiseau, 91128~~Polytechnique, Paris, France
[2]~~Laboratoire~~[2] Laboratoire d'Aérologie, CNRS/UPS, Observatoire Midi-Pyrénées, ~~14 avenue Edouard Belin,~~ Toulouse, France
[3]~~LATMOS~~[3] Atmospheric Sciences and Global Change Division, Pacific Northwest National Laboratory, Richland, Washington, USA
[4]LATMOS/IPSL, ~~Univ.~~Université Versailles Saint-Quentin en Yvelines, Guyancourt, France

Correspondence to: Artem G. Feofilov (artem.feofilov@lmd.polytechnique.fr)

Abstract~~.~~

The ~~spaceborne~~space-borne active sounders have been contributing invaluable vertically resolved information of atmospheric optical properties since the launch of ~~CALIPSO~~ (Cloud-Aerosol Lidar and Infrared Pathfinder Satellite Observation (CALIPSO) in 2006. To ~~ensure the continuity of~~ build long-term records from space-borne lidars useful for climate studies ~~and monitoring the global changes~~, one has to understand the differences between successive space lidars operating at different wavelengths, flying ~~at~~on different orbits, and ~~utilizing~~using different ~~observation~~viewing geometries, receiving paths, and detectors. In this article, we ~~show~~compare the results of ~~an intercomparison study of ALADIN~~ (Atmospheric Laser Doppler INstrument (ALADIN) and ~~CALIOP~~ (Cloud-Aerosol Lidar with Orthogonal Polarization (CALIOP) lidars ~~using their scattering ratio (SR) products~~ for the period ~~of~~from 28/06/2019~~–~~ to 31/12/2019. ~~We suggest an optimal set of collocation criteria~~ First, we build a dataset of ALADIN/CALIOP collocated profiles (Δdist < 1°; Δtime < 6h~~)~~, ~~which would give a representative set of collocated profiles~~). Then we convert the ALADIN's 355nm particulate backscatter and extinction profiles into the scattering ratio vertical profiles SR(z) at 532 nm using molecular density profiles from Goddard Earth Observing System Data Assimilation System, version 5 (GEOS-5 DAS). And finally, we build the CALIOP and ~~we show that for such~~ALADIN globally gridded cloud fraction profiles CF(z) in applying the same cloud detection threshold to the SR(z) profiles of both lidars at the same spatial resolution.

Before comparing the SR(z) and CF(z) profiles retrieved from the two analyzed lidar missions, we performed a ~~pair of instruments the theoretically~~numerical experiment to estimate the best achievable cloud detection agreement ~~for the data~~

Mis en forme : Anglais (États-Unis)
Mis en forme : Anglais (États-Unis)
Mis en forme : Anglais (États-Unis)
Mis en forme : Anglais (États-Unis)
Mis en forme : Anglais (États-Unis)
Mis en forme : Anglais (États-Unis)
Mis en forme : Anglais (États-Unis)
Mis en forme : Anglais (États-Unis)
Mis en forme : Anglais (États-Unis)
Mis en forme : Anglais (États-Unis)
Mis en forme : Couleur de police : Texte 1
Mis en forme : Couleur de police : Texte 1
Mis en forme : Couleur de police : Texte 1
Mis en forme : Couleur de police : Texte 1
Mis en forme : Couleur de police : Texte 1
Mis en forme : Couleur de police : Texte 1
Mis en forme : Couleur de police : Texte 1
Mis en forme : Couleur de police : Texte 1
Mis en forme : Couleur de police : Texte 1
Mis en forme : Couleur de police : Texte 1
Mis en forme : Couleur de police : Texte 1
Mis en forme : Couleur de police : Texte 1
Mis en forme : Couleur de police : Texte 1
Mis en forme : Couleur de police : Texte 1
Mis en forme : Couleur de police : Texte 1
Mis en forme : Couleur de police : Texte 1
Mis en forme : Couleur de police : Texte 1
Mis en forme : Couleur de police : Texte 1
Mis en forme : Couleur de police : Texte 1
Mis en forme : Couleur de police : Texte 1
Mis en forme : Couleur de police : Texte 1

$CDA_{norm}(z)$ given the fundamental differences in the two systems. We define $CDA_{norm}(z)$ in each latitude/altitude bin as the occurrence frequency of cloud layers detected by both lidars, divided by a cloud fraction value for the same latitude/altitude bin. We simulated the SR(z) and CF(z) profiles that would be observed by these two lidars if they were flying over the same atmosphere predicted by a global model. By analyzing these simulations, we show that the theoretical limit for $CDA_{norm}^{theor}(z)$ for a combination of ALADIN and CALIOP instruments is equal to 0.81±0.07 at all altitudes. In other words, 19% of the clouds cannot be detected simultaneously by two instruments due to said differences.

The analyses of the actual observed CALIOP/ALADIN collocated ~~with aforementioned criteria is 0.77±0.17. The analysis of a collocated database consisting of~~ data set containing ~78000 pairs of ~~collocated~~ nighttime SR(z) profiles revealed ~~the following~~: (a) ~~in~~the values of SR(z) agree well up to ~3km height; (b) the ~~cloud-free area, the~~CF(z) profiles show agreement ~~is good indicating low frequency of false positive cloud detections by both instruments; (b) the cloud detection agreement is~~below ~3km where ~80% of the clouds detected by CALIOP are detected by ALADIN as expected from the numerical experiment; (c) above this height, the $CDA_{norm}^{obs}(z)$ reduces to ~50%; (d) on average, better ~~for the lower layers. Above ~7 km, the ALADIN product demonstrates lower~~ sensitivity ~~because of lower backscatter at 355 nm and because of lower signal-to-noise ratio; (c) in 50% of the analyzed cases when ALADIN reported a low cloud not detected by CALIOP, the middle-level cloud hindered the observations and perturbed the ALADIN's retrieval indicating the need for quality flag refining for such scenarios; (d) large sensitivity to lower clouds leads to skewing~~to lower clouds skews the ALADIN's cloud ~~peaks down~~peak height in pairs of ALADIN/CALIOP profiles by ~0.5±0.4~~6~~ km downwards, but this effect does not alter the heights of polar stratospheric ~~cloud peak heights~~clouds and high tropical clouds thanks to their strong backscatter signals; (e) the temporal evolution of ~~cloud agreement quality~~the observed $CDA_{norm}^{obs}(z)$ does not reveal any ~~anomaly for~~statistically significant change during the considered period~~, indicating~~. This indicates that ~~hot pixels and laser degradation effects~~the instrument-related issues in ALADIN L0/L1 have been mitigated at least down to the uncertainties ~~in~~of the following ~~cloud detection agreement $CDA_{norm}^{obs}(z)$~~ values: ~~61±1668±12%, 55±14~~%, 34±~~18% 24±10%, 26±1014~~%, 39±13%, and ~~22±12%~~42±14% estimated at 0.75 km, 2.25 km, 6.75 km, 8.75 km, and 10.25 km, respectively.

1 Introduction

Clouds play an important role in the energy budget of our planet: optically thick clouds reflect the incoming solar radiation, leading to cooling of the Earth, while thinner clouds act as "greenhouse films", preventing escape of the Earth's long-wave radiation to space. Climate feedback analyses ~~reveal~~show that clouds are a large source of uncertainty for the climate sensitivity of climate models and, ~~therefore~~so, for the ~~predicted~~future climate ~~development scenarios~~evolution (e.g. Nam et al., 2012; Chepfer et al., 2014; Vaillant de Guélis et al., 2018~~).~~.; Zelinka et al., 2020). Understanding the Earth's ~~radiative~~ energy budget requires knowing ~~the cloud cover, their~~cloud's coverage, geographical and ~~altitudinal~~vertical distribution, temperature, ~~composition, as well as the~~ and optical properties ~~of cloud particles and their concentration.~~ .

Mis en forme : Couleur de police : Texte 1
Mis en forme : Couleur de police : Texte 1
Mis en forme : Couleur de police : Texte 1
Mis en forme : Couleur de police : Texte 1
Mis en forme : Couleur de police : Texte 1
Mis en forme : Couleur de police : Texte 1
Mis en forme : Couleur de police : Texte 1, Indice
Mis en forme : Couleur de police : Texte 1
Mis en forme : Couleur de police : Texte 1
Mis en forme : Couleur de police : Texte 1
Mis en forme : Couleur de police : Texte 1
Mis en forme : Couleur de police : Texte 1
Mis en forme : Couleur de police : Texte 1
Mis en forme : Couleur de police : Texte 1
Mis en forme : Couleur de police : Texte 1

Satellite observations have been providing a continuous survey of clouds over the whole globe. ~~IR~~Infrared sounders have been observing our planet since 1979: from the ~~TOVS (~~TIROS Operational Vertical Sounder (TOVS) instruments (Smith et al., 1979) onboard the National Oceanic and Atmospheric Administration (NOAA) polar satellites to the ~~AIRS (~~Atmospheric InfraRed Sounder (AIRS) spectrometer (Chahine et al., 2006) onboard Aqua (since 2002) and to the ~~IASI (~~Infrared Atmospheric Sounder Interferometer (IASI) instrument (Chalon et al., 2001; Hilton et al., 2012) onboard MetOp (since 2006), with increasing spectral resolution. Despite an excellent daily coverage and daytime/nighttime observation capability (Menzel et al., 2016; Stubenrauch et al., 2017), the height uncertainty of the cloud products retrieved from the observations performed by these ~~spaceborne~~space-borne instruments is ~~limited by~~large (e.g. Feofilov and Stubenrauch, 2017). This precludes the ~~width~~retrieval of ~~their channels' contribution functions, which is on the order of hundreds of meters, and the~~ the cloud's vertical profile ~~of the cloud cannot be retrieved~~ with the accuracy needed for climate relevant processes and feedback analysis. This drawback ~~is eliminated by~~does not exist for active sounders, ~~the very nature of~~ which ~~is based on~~measure the altitude-resolved ~~detection~~profiles of backscattered radiation~~, and~~ with accuracy on the order of 1E0-1E2 meters. Among them, one can name the ~~vertical profiles of the cloud parameters are available from the CALIOP (~~Cloud-Aerosol Lidar with Orthogonal Polarization (CALIOP) lidar (Winker et al., 2003, 2004, 2007, 2009, 2010) and CloudSat radar (Stephens et al., 2002~~);~~ 2009), which have been providing vertically resolved cloud and aerosol properties since 2006~~,~~. The CATS (Cloud-Aerosol Transport System) lidar on-board ISS provided measurements for over 33 months starting from the beginning of 2015 (McGill et al., 2015). The ~~ALADIN (~~Atmospheric Laser Doppler INstrument (ALADIN) lidar on-board Aeolus (Krawczyk et al., 1995; Stoffelen et al., 2005; ADM-Aeolus Science report, 2008) has been measuring horizontal winds and aerosols/clouds since September 2018. More lidars are planned – in 2023, the ~~ATLID (~~ATmosperic LIDar (ATLID)/EarthCare instrument (Héliere et al., 2012) will be launched and other space-borne lidars are in the development phase. ~~Even though all~~All active instruments share the same measuring principle – a short pulse of laser or radar electromagnetic radiation is sent to the atmosphere and the time-resolved backscatter signal is collected by the telescope and is registered in one or several receiver channels. However, the wavelength, pulse energy, pulse repetition frequency (PRF), telescope diameter, orbit, detector, and many other parameters are not the same for any ~~given~~ pair of ~~current or future~~ instruments. These differences ~~are responsible for~~define the active instruments' capability of detecting atmospheric aerosols and/or ~~hydrometeors~~clouds for a given atmospheric scenario and observation conditions (day, night, averaging distance). At the same time, there is an obvious need of ensuring the continuity of global ~~spaceborne~~space-borne measurements and ~~obtaining~~of getting a ~~seamless~~smooth transition between the satellite missions (~~Chepher~~Winker et al.~~,~~. 2017; Chepfer et al., 2014, 2018).

This ~~works~~work seeks to address this issue using ALADIN/Aeolus ~~spaceborne~~space-borne wind lidar operating at 355 nm and CALIOP/CALIPSO atmospheric lidar operating at 532 nm. Even though the ~~main~~primary goal of ALADIN is wind detection (Reitebuch et al., 2020; Straume et al., 2020), ~~the calibration of which does not rely on absolute calibration of the detected radiation,~~ its products include profiles of atmospheric optical properties ~~and such a comparison serves the intercalibration purposes.~~. In addition, the methods developed in ~~the course of~~ this study~~,~~ and ~~the interpretation of the~~

~~results~~its conclusions will set the stage for the future ~~validation~~comparison of the ATLID/EarthCare ~~instrument and~~observations with other ~~spaceborne~~space-borne lidars.

The structure of the article is as follows. In Section 2, we describe the datasets used in this study~~;~~ and explain the collocation criteria~~, and provide an estimate~~. Section 3 provides the definitions and the basic formulae needed for comparison of two lidars operating at different wavelengths. In Section 4, we describe the numerical experiment aimed at the estimation of the best possible theoretically achievable cloud detection agreement for ~~two instruments in given configuration. In Section 3, we strive~~the cloud fraction profiles retrieved from CALIOP and ALADIN observations. Section 5 is dedicated to ~~provide a multifaceted view of~~the analysis of the results and to the discussion of similarities and differences between the collocated ~~dataset~~SR profiles and ~~discuss the observed differences.~~cloud fraction distributions. Section ~~4~~6 concludes the article.

~~**2 Datasets and methods**~~

2 Data

We start this section with the description of ALADIN/Aeolus optical properties dataset, followed by the description of CALIOP/CALIPSO product ~~and its modification aimed at matching the sampling and averaging of Aeolus product~~. In the next steps, we define the procedures and criteria for the comparison of these two products.

2.1 AEOLUS

~~A detailed description of the Aeolus mission and its instrument can be found in (Krawczyk et al., 1995; Stoffelen et al., 2005; ADM-Aeolus Science report, 2008; Flamant et al., 2017) and here~~ In this work, we provide only a brief description of the lidar and the details necessary for understanding the key differences between the compared instruments. For a detailed description of the Aeolus mission and its instrument, we refer the reader to (Krawczyk et al., 1995; Stoffelen et al., 2005; ADM-Aeolus Science report, 2008; Flamant et al., 2017). The Aeolus satellite carries a Doppler wind lidar called ALADIN, which operates at 355 nm wavelength and is composed of a transmitter, a Cassegrain telescope, and a receiver capable of separating the molecular (Rayleigh) and particular (Mie) backscattered photons (~~HSRL,~~ high spectral resolution lidar, HSRL). The lidar ~~is aimed~~ observes the atmosphere at 35° from nadir and ~~90°~~perpendicular to the satellite track, its orbit is inclined at 96.97°, and the instrument overpasses the equator at 6h and 18h of local solar time (LST), see also Fig. 1 and Table 1 to compare with CALIOP.

The laser emitter of the lidar sends 15 ns long pulses of 355 nm radiation down ~~into~~to the atmosphere 50 times per second. The ~~telescope~~lidar optical system collects the ~~light that is~~ backscattered photons, which are then registered in the instrument's Rayleigh and Mie channels. The wind detection is performed with the help of interferometric technique from ~~air molecules, aerosols and hydrometeors. The received backscatter signal in Mie receiver passes through a Fizeau interferometer, which produces a linear fringe whose position~~the image formed on the ~~ACCD (~~Accumulation Charge

Coupled Device~~) detector of this channel is linked to the wind velocity. As for the Rayleigh receiver, it uses a dual-filter Fabry–Pérot interferometer, which throws two images on the ACCD detector of this channel, and the wind speed is defined from the ratio~~ (ACCD) detectors of ~~intensity of these two images~~the lidar (Chanin et al., 1989). Besides the winds, the Aeolus processing algorithms retrieve the optical properties of the observed atmospheric layers (Ansmann et al., 2007; Flamant et al., 2017). The vertical resolution of the instrument is adjustable, but the total number of points in a vertical profile is ~~defined by~~equal to 24, that corresponds to a number of rows ~~of the detector dedicated to this purpose (24).~~in ACCD. The observation priorities changed throughout the period of the mission (Bley et al., 2021), and for ~~the majority~~most of the period considered in this work (see below), the vertical sampling of both Mie and Rayleigh channels between 2 km and 22 km was equal to 1 km whereas the sampling below 2 km varied from 0.25 to 1 km. The native horizontal resolution of 140 m of the instrument is sacrificed to achieve higher signal ~~–~~ to ~~–~~ noise ratio (SNR) both onboard by accumulating the detected profiles and on the ground by averaging the downloaded profiles at different steps of the processing chain (Flamant et al., 2017).

~~The present study has been done using the pilot L2A dataset from Aeolus, Prototype_v3.10, which is available~~ALADIN is a relatively new instrument, and its calibration/validation activity is still on the way (Baars et al., 2020; Donovan et al., 2020; Kanitz et al., 2020; Reitebuch et al., 2020; Straume et al., 2020). This includes, but is not limited to internal calibration and comparisons with other observations. The Aeolus mission faced several technical issues, which hindered getting the planned specifications. These issues are related to several factors: (a) laser power degradation (60 mJ/pulse instead of 80 mJ/pulse) and signal losses in the emission and reception paths (33%) that results in lower SNR than planned, (b) telescope mirror temperature effects biasing the wind detection and calibration of Mie and Rayleigh channels of ALADIN, (c) constantly increasing number of hot pixels of both ACCD detectors (Weiler et al., 2021) leading to errors both in wind speed and in retrieved optical parameters of the atmosphere. The Aeolus teams mitigated at least some of these adverse effects (e.g. Baars et ql., 2020; Weiler et al., 2021), and it would be interesting to see whether the pilot L2A dataset, Prototype_v3.10 is free of cloud detection quality trends.

We have performed the present study using the pilot L2A dataset from Aeolus, Prototype_v3.10, which is available for participating Cal/Val teams for a limited period of ALADIN's observations, from 28/06/2019 through the 31/12/2019. According to (Flamant et al., 2008, 2017), the L2A data is ~~produced~~retrieved from the L1B product of this instrument and it contains height profiles of Mie and Rayleigh co-polarized backscatter and extinction coefficients, scattering ratios~~,~~ (SR), and lidar ratios ~~(Flamant et al., 2008; Lolli et al., 2013)~~ along the lidar line-of-sight~~.~~ (Flamant et al., 2017; Lolli et al., 2013). For each vertical profile corresponding to a slant path in Fig. 1, we extracted the ~~end user, the~~SR, backscatter, and extinction profiles ~~are provided both on observation scale (87 km averages) and on smaller scales after applying scene classification, but~~calculated by standard correct algorithm (Flamant et al., 2017). As for the ~~purposes~~SR, we draw the reader's attention to the definitions and conversion formulae given below in Section 3.2. The horizontal resolution of ~~the present work the scattering ratio on the scale of 87 km~~this product is ~~an optimal choice.~~ 87 km.

In Fig. 1(a-c), we show the observation geometry and sampling of ALADIN's L2A product as well as three variables retrieved from its observations, namely, the APB (Attenuated Particular Backscatter), the AMB (Attenuated Molecular Backscatter), and the ATB (Attenuated Total Backscatter). The white dashed lines in Fig. 1 represent the lines of sight of the instrument. One has to note, however, that in the real life the ALADIN's line of sight is pointed perpendicular to the flight direction; at the same time, the horizontal variability of the observed scene is nearly the same in latitudinal and longitudinal directions at 100 km distance, so the sketch gives an idea of the comparability of the physical parameters observed by ALADIN (Fig. 1a-c) and CALIOP (Fig. 1d). The atmospheric scene used in Fig. 1 has been calculated for demonstration purposes for two wavelengths, 355 nm (Fig.1a,b,c) and 532 nm (Fig.1d) from the output of the EAMv1 (Energy Exascale Earth System Model (E3SM) atmosphere model version 1) atmospheric model (The important companions of these profiles are quality flag columns. For our analysis, we kept only the layers, which are marked either by a high Mie SNR flag or by high Rayleigh SNR flag, and by a flag indicating an absence of signal attenuation. These flags are necessary and sufficient for valid extinction, backscatter, and SR(z) profiles, which we use in the analysis.

Rasch et al., 2019) for the conditions of autumn equinox in Northern hemisphere. This data has been obtained with the help of the COSP2 (the Cloud Feedback Model Intercomparison Project Observational Simulator Package, v2) package, which is capable of simulating the atmospheric observables for spaceborne instruments (Swales et al., 2018). The CALIOP is built into COSP2 (Chepfer et al., 2008) whereas the ALADIN is not yet a part of this package, so we used the 355 nm calculations by COSP2 (Reverdy et al., 2015) at fine grid corresponding to ALADIN's original laser pulse frequency rate and modified them in accordance with the ALADIN's vertical and horizontal averaging. The cloud variability along the satellite's track has been estimated from the gridded EAMv1 data using the parameterization of (Boutle et al., 2014). Figure 1 also serves as an illustration to theoretically achievable cloud detection agreement discussed below.

For each profile corresponding to an inclined dashed line in Fig. 1, we extracted the corresponding scattering ratio (SR) column of *sca_optical_properties* group of variables where SCA stands for standard correct algorithm (Flamant et al., 2017). An important companion of such a column is a corresponding quality flag column, which we scanned looking for the points characterized either by high Mie signal-to-noise ratio (SNR) or by high Rayleigh SNR, and by a flag that indicates an absence of signal attenuation. Presumably, these flags are necessary and sufficient for a valid SR profile, which can be then compared with that of CALIOP.

2.2 CALIPSO-GOCCP

CALIOP, a two-wavelength polarization-sensitive near nadir viewing lidar, provides high-resolution vertical profiles of aerosols and clouds. (Winker et al., 2004, 2007, 2009). Its orbital altitude is 705 km and the orbit is inclined at 98.05º and it. The lidar overpasses the equator at 1h30 and 13h30 LST, see also Table 1 and the left-hand-side parts of Fig. 1 panels. It uses three receiver channels: one measuring the 1064 nm backscatter intensity and two channels measuring orthogonally polarized components of the 532 nm backscattered signal. Cloud and aerosol layers are detected by comparing the measured 532 nm signal return with the return expected from a molecular atmosphere. (see the definitions in Section 3.2).

The ~~CALIPSO-GOCCP~~General Circulation Model (GCM) Oriented Cloud Calipso Product (CALIPSO-GOCCP) was initially designed to evaluate GCM cloudiness ~~(Chepfer et al., 2010).~~. It is derived from CALIPSO L1/NASA products at Laboratory of Dynamic Meteorology (LMD~~/~~) and Institute of Pierre-Simon Laplace (IPSL) with the support of NASA/CNES, ICARE~~,~~ Thematic Center (Lille, France), and ClimServ data service (IPSL) and it contains observational cloud diagnostics including the instantaneous scattering ratio (profiles) at the native horizontal resolution of CALIOP (333 m) and at ~~~0.5 km~~480m vertical resolution~~.~~ (Chepfer et al., 2008, 2010, 2012). This makes it a good reference dataset for ALADIN retrievals because ~~it~~one can ~~be~~ easily ~~recalculated~~ recalculate it to ~~the latter's~~ALADIN's horizontal and vertical grids ~~considering the corresponding horizontal~~through averaging~~. Since the CALIOP is not a HSRL, the detailed information on AMB~~ along the track and ~~APB is not available, and one has to compare the SR products. Correspondingly, we convert the ALADIN's SR retrieved at 355 nm to SR at 532 nm using the following equation:~~in vertical bins, respectively.

~~$SR_{532} = SR_{355} \times 3.3 - 2.3$ (1)~~

~~which is derived from (Collis and Russell, 1976) in an assumption that their fitting parameter A (see their Section 4.3.1) is equal to 3. The choice of the fitting parameter is not crucial for the purposes of the present work because the conversion described by Eq. 1 is linear and it does not change the altitude distribution of the SR. On the other hand, using the same physical parameter is highly advisable for the comparisons we are intending to perform. Theoretically, one could have validated the parameters of Eq. 1 using the collocated data under consideration, but, looking ahead, one can say that the spread of the values is too large to do it with reasonable uncertainty, so we will stay with Eq. 1 in the framework of this paper and in Appendix A we justify our choice of conversion coefficients using the collocated data.~~

~~**2.3 Collocation criteria**~~

2.3 Collocation of AEOLUS and CALIPSO profiles

Figure 1 illustrates the orbit and overpass time differences between the two lidars. In Fig. 1b, AEOLUS overflies the same area as was measured by CALIOP ~4.5 h earlier (Fig. 1a). We recall here, that the ALADIN's line of sight is pointed at 35° to nadir and perpendicular to the flight direction (purple slant paths in the right-hand side parts of Fig. 1 panels) whereas the CALIOP probes the atmosphere in near nadir mode (3° off nadir). As for any collocation, there is a trade-off between the quality of collocation and the number of collocated pairs of profiles. As we show below, ~~in the case of~~for AEOLUS and CALIPSO, one has to supplement this tradeoff ~~is supplemented~~ with a requirement of a representative geographical coverage, because imposing a ~~strict~~stricter temporal overlap criterion ~~dramatically changes~~adversely affects the latitudinal distribution of the collocated points. Since the horizontal averaging and resolution of the Aeolus Prototype_v3.10 product is 87 km, there is ~~no~~not much sense in collocating the data with the accuracy better than this value. On the other hand, a fractional standard deviation f_c of cloud water content at 1º (~111 km) distance is about 0.5 for a cloud cover of 1 (Boutle et al., 2014), and there is a risk of comparing incoherent quantities, so we took Δdist = 1º as a limit for the collocations and created several subsets based on the Δtime, the absolute value of the difference between the two collocated measurements. In

Fig. 2, we show ~~three~~six such subsets, and the Table 2 provides the ~~information about the other cases we considered.~~total number of collocations for each of them. On the one hand, one can see that a strict collocation criterion of Δtime < 1h (black curve in Fig. ~~2a~~2) provides the information only about two narrow zones in the Southern and Northern polar regions. On the other hand, an excellent ~~geographical~~latitudinal coverage ~~shown~~corresponding to Δtime < 24 h (dashed magenta curve in Fig. ~~2c~~2) comes at the cost of mixing up the cases, which differ by almost one day that is unacceptable from the point of view of temporal variation. ~~In addition, this case is characterized by unequal distribution of Δtime throughout the globe.~~ Finally, we have chosen for the analysis a subset corresponding to Δtime < 6h ~~(Fig. 2b) has been chosen for the analysis.~~. Over the oceans, the diurnal effects in cloud distribution associated with this ~~difference~~delay are small (e.g. ~~Noel~~Noël et al., 2018; Chepfer et al., 2019; Feofilov and Stubenrauch, 2019) and the land represents just one third of the analyzed cases. ALADIN observes the atmosphere in dusk-dawn mode whereas CALIPSO has a clear separation between the daytime and the nighttime observations (Fig. 1). To avoid the risks associated with the solar contamination, we picked up only the collocations, which correspond to night-time ~~cases, which yield~~CALIPSO observations. This yielded about 7.~~8E4~~7E4 pairs of SR profiles. In supplementary materials~~,~~ (Feofilov et al., 2021), we provide the complete collocated database, which corresponds to the last line, 4th column of Table 2 (3.~~7E5~~2E5 collocations), for further analysis by the interested teams.

~~2~~3 Method

3.1 Lidar equation

An atmospheric lidar sends a short pulse of laser radiation directed towards the atmosphere. The lidar optics collects the backscattered photons and drives them to a detector. The detected signal is time-resolved, and each time bin corresponds to a fixed distance from the lidar to the certain atmospheric layer. AEOLUS wavelength of emission is 355nm while CALIPSO's is 532nm. In the atmosphere, the photons coming from the lidar can be backscattered by the molecules, which are much smaller than the wavelength of our two lasers (Rayleigh scattering), by the aerosol particles, which are comparable to or larger than the wavelengths of our two lasers, and by the coarse aerosol and cloud particles, which are much larger than the wavelengths of our two lasers (Mie scattering). These processes are characterized by the corresponding wavelength-dependent backscatter coefficients $\beta_{mol}(\lambda, z)$ and $\beta_{part}(\lambda, z)$ measured in [m^{-1} sr^{-1}]. The attenuation of the laser beam along its path within each layer is characterized by extinction coefficients $\alpha_{mol}(\lambda, z)$ and $\alpha_{part}(\lambda, z)$ in [m^{-1}]. On their pathway in the atmosphere, the photons are also scattered in other directions than backscatter and then collected in the telescope after multiple scatterings. The total lidar attenuated backscattered signal (ATB) corrected for geometrical effects and normalized to molecular signal is usually written as:

$$ATB(\lambda, z) = (\beta_{mol}(\lambda, z) + \beta_{part}(\lambda, z)) \times e^{-2\int_{z_{sat}}^{z}(\alpha_{mol}(\lambda,z\prime)+\eta\alpha_{part}(\lambda,z\prime))dz\prime} \quad (1)$$

where Z_{sat} is the altitude of the satellite, λ is the wavelength, and η is a multiple scattering coefficient, which depends on the lidar configuration and is set to 0.7 for CALIOP (see (Winker, 2003; Chiriaco et al., 2006; Chepfer et al., 2008; Garnier et al., 2015; Reverdy et al., 2015) for the discussion of this value).

3.2 Two definitions of scattering ratio profile

To highlight particles in an atmospheric layer versus molecular background, one often uses the "scattering ratio" or SR. But, two different definitions of SR exist in the literature, and in particular, the ALADIN documents and CALIPSO documents do not use the same definition. So, we provide both definitions and explain our choice below. The first one relates only to scattering properties of the medium and is used in ALADIN product (Flamant et al., 2017):

$$SR^A(\lambda,z) = \frac{\beta_{mol}(\lambda,z)+\beta_{part}(\lambda,z)}{\beta_{mol}(\lambda,z)} \quad (2)$$

According to this definition, $SR^A(\lambda,z)$ is strictly equal to or greater than unity and its interpretation is straightforward: the larger the number, the stronger is the contribution of particles to backscattered signal. But, this definition requires knowledge of both $\beta_{mol}(\lambda,z)$ and $\beta_{part}(\lambda,z)$, which available from ALADIN observations thanks to its HSRL capability (see Section 2.1) but not from non-HSRL lidars such as CALIPSO (see Section 2.2).

The second definition is closer to the profiles observed by classic non-HSRL lidars and is used in CALIPSO products (e.g. Chepfer et al., 2008, 2013):

$$SR^C(\lambda,z) = \frac{ATB(\lambda,z)}{AMB(\lambda,z)} \quad (3)$$

where $ATB(\lambda,z)$ is the total attenuated backscatter given by Eq. 1 and $AMB(\lambda,z)$ is the attenuated molecular backscatter estimated in the absence of particles:

$$AMB(\lambda,z) = \beta_{mol}(\lambda,z) \times e^{-2\int_{Z_{sat}}^{z} \alpha_{mol}(\lambda,z')\,dz'} \quad (4)$$

The $ATB(\lambda,z)$ values in Eq. 3 are measured by a lidar and the profile of $AMB(\lambda,z)$ can be estimated from Eq. 4 if the molecular density profile is known. Since the exponential part in the enumerator of Eq. 1 leads to a significant attenuation in the presence of particles, the value of $SR(\lambda,z)$ can be less than unity below a thick cloud layer. The definition (Eq. 4) is convenient for the lidars, which cannot distinguish the molecular and particulate components of the backscattered signals. Since the CALIOP is such a lidar, we will use this very definition in the present work as it was done before (Chepfer et al., 2008, 2013). Correspondingly, here and below $SR(\lambda,z) = SR^C(\lambda,z)$. In the rest of the paper, we use the definition of $SR(\lambda,z) = SR^C(\lambda,z)$ given in Eq. 3 and we do not use the $SR^A(\lambda,z)$ given in Eq. 2.

3.3 Calculating averaged SR(z) profiles from CALIOP data

Since we used a high-resolution CALIOP data on a 333m grid, a direct comparison with ALADIN L2 product with its 87 km averaged data was not possible. To calculate the averaged CALIOP $SR(z)$, we took the original $ATB(z)$ and $AMB(z)$

profiles, averaged them in the ±40 km vicinity of the point defined as the closest one to ALADIN's track, and got the $SR(z)$ (Eq. 3). This averaging with a subsequent application of a SR threshold may lead to an overestimation of the cloud fraction in the boundary layer, for a field of optically thick geometrically small liquid clouds (e.g. cumulus), but this overestimation will be the same for both instruments.

3.4 Estimating ~~the theoretically achievable~~ SR(z) profiles at 532 nm from ALADIN data

After having stated the SR definition (Eq. 3) that we will use to compare the observations collected by the two instruments, we now need to consider their wavelength differences. Indeed, the SR(z) profile is wavelength-dependent as $\alpha_{mol}(\lambda, z)$, $\alpha_{part}(\lambda, z)$, $\beta_{mol}(\lambda, z)$, $\beta_{part}(\lambda, z)$ and, therefore, $ATB(\lambda, z)$, $AMB(\lambda, z)$ depend on the wavelengths. Therefore, one needs to convert the first instrument's SR values to those of the second one, or vice versa. Leaping ahead, we say that since ALADIN can distinguish the molecular backscatter from the particulate one, it provides more information, so it is better suited for the conversion than CALIOP. Below, we provide the formalism used for the conversion (Collis and Russell, 1976; Bucholz, 1995) as well as the corresponding variable values calculated at two wavelengths, 355 and 532 nm. For the molecular backscatter:

$$\beta_{mol}(\lambda, z) = (d\sigma/d\Omega)_{\lambda} \times N(z);\ \alpha_{mol}(\lambda, z) = \frac{4\pi}{1.5}\beta_{mol}(\lambda, z) \quad (5)$$

$$(d\sigma/d\Omega)_{\lambda} = \frac{\sigma(\lambda,z)}{4\pi} \times \frac{3}{4}(1 + cos^2(\pi)) \quad (6)$$

$$\sigma(\lambda, z) = \frac{24\pi^3 (n_s^2(\lambda)-1)^2 (6+3\rho(\lambda))}{\lambda^4 N_s^2 (n_s^2(\lambda)+2)^2 (6-7\rho(\lambda))} \quad (7)$$

where $(d\sigma/d\Omega)_{\lambda}$ is a differential cross section [m^2 sr^{-1}], $N(z)$ is a number density [m^{-3}], $\sigma(\lambda, z)$ is Rayleigh cross section [m^2], $n_s(\lambda)$ is the refractive index for standard air, $\rho(\lambda)$ is the depolarization factor, and N_s is the number density of standard air (2.54743×10^{25} m^{-3}). We estimated the $n_s(\lambda)$ values according to (Ciddor, 1996) and obtained $n_s(355nm) = 1.00028571$ and $n_s(532nm) = 1.00027821$. We took the $\rho(\lambda)$ values from Table 1 of (Bucholz, 1995) according to which $\rho(355nm) = 3.01 \times 10^{-2}$ and $\rho(532nm) = 2.84 \times 10^{-2}$. The corresponding values of $(d\sigma/d\Omega)_{\lambda}$ at 355nm and 532nm are then 3.2897988×10^{-31} m^2 sr^{-1} and 6.1668318×10^{-32} m^2 sr^{-1}, respectively. For the particulate backscatter, we took advantage of the fact that the extinction and backscatter coefficients $\alpha_{part}(\lambda, z)$ and $\beta_{part}(\lambda, z)$ barely change at these wavelengths for large particles. Using a known molecular density profile from GEOS-5 DAS (Goddard Earth Observing System Data Assimilation System, version 5), see (Rienecker, 2008), and estimating the $AMB(532nm, z)$ and $ATB(532nm, z)$ values from Eqs. 1, 2 and Eqs. 4–7, we finally get the $SR'(532nm, z)$ profile for ALADIN, which is comparable with the $SR(532nm, z)$ of the CALIOP.

3.5 Cloud detection, cloud fraction, and normalized cloud detection agreement

In this work, we define the "cloud" to be present in the atmospheric layer z±Δz when the following condition fulfills (Chepfer et al., 2013):

$$SR(532nm, z) > 5 \quad (8)$$

For cloud detection, we deliberately do not apply the second criterion of (Chepfer et al., 2013):

$$ATB(532nm, z) - ATB(532nm, z) > 2.5 \times 10^{-6}\, m^{-1} sr^{-1} \quad (9)$$

because of two reasons: (a) this criterion was introduced in (Chepfer et al., 2013) to filter noise in individual profiles at native resolution (1/3km along track), whereas in this work we use the $SR(532nm, z)$ averages recalculated from ATB and AMB over ~80 km distance along-track and (b) this would have adversely affected the high cloud amount of ALADIN. Even though this definition makes the CALIOP clouds inconsistent with their definition in current CALIPSO products, this allows estimating the potential capabilities of ALADIN for cloud detection. If a given atmospheric layer was observed multiple times, we define the cloud fraction (CF) in a usual way:

$$CF(z) = \frac{N_{cld}(z)}{N_{tot}(z)} \quad (10)$$

where $N_{cld}(z)$ is a number of times the condition of Eq. 8 fulfills and $N_{tot}(z)$ is a total number of measurements in this layer. As for cloud detection agreement and disagreement, we distinguish four cases: when both CALIOP and ALADIN detect a cloud, when neither of them detects a cloud, when CALIOP detects a cloud whereas ALADIN misses it, and when ALADIN detect a cloud whereas CALIOP misses it. We will name these cases as YES_YES, NO_NO, YES_NO, and NO_YES, and will define their occurrence frequencies as:

$$R_{YES\_YES}(z) = \frac{N_{YES\_YES}(z)}{N_{tot}(z)}; R_{NO\_NO}(z) = \frac{N_{NO\_NO}(z)}{N_{tot}(z)}; R_{YES\_NO}(z) = \frac{N_{YES\_NO}(z)}{N_{tot}(z)}; R_{NO\_YES}(z) = \frac{N_{NO\_YES}(z)}{N_{tot}(z)} \quad (11)$$

The first term in Eq. 11 corresponds to cloud detection agreement ($CDA(z)$), which we will also use in its normalized form, $CDA_{norm}(z)$:

$$CDA_{norm}(z) = \frac{CDA(z)}{CF(z)} = \frac{N_{YES\_YES}(z)}{N_{cld}(z)} \quad (12)$$

As follows from these definitions, if $CF(z)$ is greater than zero and $CDA_{norm}(z)$ is equal to 1 then there is a perfect agreement between ~~two collocated datasets~~ the clouds retrieved from both instruments. In the same way, if $CF(z)$ is greater than zero and $CDA_{norm}(z)$ is equal to 0 then there is no agreement.

Mis en forme : Normal

~~To justify the~~ 4. Theoretical estimate of the best achievable cloud detection agreement between ALADIN and CALIOP

The aforementioned differences between the missions prevent that the two lidars will observe the same clouds at the same time, except for the polar zonnes. Knowing the differences in the orbits, wavelengths, and spatial resolution, one can carry out a numerical experiment aimed at the estimation of the best achievable agreement $CDA^{theor}(z)$ and $CDA^{theor}_{norm}(z)$ that one can expect for a combination of these two missions.

4.1 Setup of the numerical experiment

To estimate the theoretically possible cloud detection agreement for a considered combination of two lidars and for the chosen collocation criteria ~~and to estimate the theoretically possible agreement for the clouds detected by two instruments in a given setup and for the selected Δtime and Δdist values, we have~~, we performed ~~a~~the following numerical experiment ~~using the same calculated data as we used~~outlined in a flowchart in Fig. ~~1. This time, we picked up the "lidar curtain" at 532 nm calculated at the resolution of CALIOP (333m) and~~ 3. First, we created a gridded atmosphere from the output of the U.S. Department of Energy's Energy Exascale Earth System Model (E3SM) atmosphere model (EAM) version 1 (EAMv1; Rasch et al., 2019) for the conditions of autumn equinox in Northern hemisphere. ~~artificial pairs of "collocated" data with the Δdist distribution modulated by that of a real collocated dataset. The "reference", CALIOP profile has been composed using 2000 individual SR profiles covering 67 km region that is somewhat less than the 87 km~~ This subset does not contain winter atmosphere possible for the period covered by Aeolus Prototype_v3.10 dataset, but it is representative enough from the point of view of the cloud fraction profiles and their variability since it presents a snapshot of both hemispheres, pole-to-pole. From this data, we created a set of daily orbits or "lidar curtains" at the resolution of CALIOP (333m). Since the resolution of EAMv1 data is coarser than that of CALIOP, we estimated the subgrid cloud variability along the satellite's track using the parameterization of (Boutle et al., 2014) and added it to the data.

Then we fed this high-resolution atmospheric input to the Cloud Feedback Model Intercomparison Project Observational Simulator Package, v2 (COSP2) simulator, which calculates the atmospheric observables for space-borne instruments (Swales et al., 2018). ~~ALADIN. This averaging is supposed to catch the mean atmospheric properties and at the same time it is not supposed to go too far from the ALADIN footprint location. The "test" SR profile was created from the SR averages, considering both the ALADIN's off-nadir pointing and its 87 km averaging.~~The CALIOP simulator is built into COSP2 (Chepfer et al., 2008) whereas the ALADIN simulator is not yet a part of this package, so we used the 355 nm calculations by COSP2 (initially developed for ATLID Reverdy et al., 2015) at fine grid corresponding to ALADIN's original laser pulse frequency rate. To imitate the diurnal variation, we modulated the SRs using the 6-hour diurnal cycle amplitudes for land and ocean retrieved from active and passive observations (~~Noel~~Noël et al., 2018; Chepfer et al., 2019; Feofilov and Stubenrauch, 2019~~) and added them to~~). With these two high-resolution simulations in hand, we created simulated pairs of "collocated" data with the ~~comparison~~Δdist distribution modulated by that of a real collocated dataset. Then we averaged the high-resolution profiles over ~80 km distance. Besides testing ~~a~~ noise-free ~~simulations~~simulations, we also checked the effects introduced by instrumental noise ~~for CALIOP. Since ALADIN is not yet part of COSP2, we used the estimates from (Ansmann et al., 2007).~~, which we estimated from the uppermost parts of measured profiles. For both instruments, these measurements are cloud-free and the molecular return is supposed to be smooth. Correspondingly, we estimated it by a least-square fit to measured molecular return and subtracted from the profile. The root-mean-square of the remaining difference gave us a noise level, which we used in the simulations. For CALIOP, the noise level obtained for instantaneous measurements was scaled in accordance with the averaging distance (see Section 3.3). Overall, we considered about 1E5

pairs of pseudo-collocated ~~data and we present the results of cloud detection in~~ averaged profiles of $SR(532nm, z)$ and $SR'(532nm, z)$. Using these pairs and applying the same cloud detection threshold (Eq. 8), we estimated the cloud fraction profiles (Eq. 10) and the occurrence frequency profiles for the simultaneous cloud detection by both instruments (Eq. 11). Finally, we estimated the normalized cloud detection agreement (Eq. 12).

4.2 Theoretically achievable cloud detection agreement

In Fig. ~~3. We define the cloud detection agreement as follows: for each altitude bin, the cloud detection agreement is a ratio of a number of cases when both instruments have detected a cloud (SR>5) to a total number of joint observations. For a given altitude bin, the cloud amount is a ratio of number of cases with SR>5 to a total number of profiles for a single instrument, and the normalized cloud detection agreement is a ratio of the former to the latter. As one can see, the normalized cloud detection quality is~~4, we show the profiles of $CF^{theor}(z)$, $CDA^{theor}(z)$, and $CDA^{theor}_{norm}(z)$ estimated in the approach outlined above. To address the contribution of different processes to the cloud detection agreement, we show both the simulations performed with the instrumental noise and diurnal variation and the simulations performed without these perturbations. As one can see, both the $CDA^{theor}(z)$ and $CDA^{theor}_{norm}(z)$ are mostly defined by a horizontal variability of aerosols/~~hydrometeors and by~~clouds combined with differences in viewing geometries of two instruments. Observation noise and diurnal variation play the secondary role~~, and according to our estimates the saturation effects in 355 nm and 532 nm channels associated with opaque clouds (Guzman et al., 2017) do not add more than 2% to the cloud detection mismatch (not shown in Fig. 3 for the sake of clarity). Overall, the theoretically achievable agreement for the collocated data in a given setup can be estimated as 0.77±0.17 for cloud detection.~~ (compare the curves with and without variations or "noise" in Fig. 4). Overall, we estimate the mean value of the theoretically achievable normalized cloud detection agreement $CDA^{theor}_{norm}(z)$ for the collocated data in the outlined setup to be equal to 0.81±0.07. As one can see, the vertical profile of $CDA^{theor}_{norm}(z)$ does not change much with altitude, indicating that the primary sources of discrepancy are the observation geometry and the spatial variability of clouds combined with the chosen collocation criterion. If the noise were the primary source of discrepancy, we would observe a decrease of $CDA^{theor}_{norm}(z)$ profile with height. In Sections 5.3 and 5.5, we will use the theoretical limit of 0.81±0.07 obtained in this section as a benchmark.

~~3 Results and discussion~~

~~3~~5. Analysis of the ALADIN and CALIPSO observations

5.1 ~~Zonal~~Comparing zonal averages of SR profiles

Mis en forme : Titre 1

To give a general overview of the agreement between ~~two products,~~the $SR(532nm, z)$ and $SR'(532nm, z)$, we have split the ~~database~~collocated data to latitudinal zones: 90S−60S, 60S−30S, 30S−30N, 30N−60N, 60N−90N (Fig. ~~4). As it was stated above, we rescale the SR_{355} values retrieved from ALADIN observations to SR_{532} using Eq. 1. Even though the zonal mean statistics does not imply using collocated data, we do it to avoid any incoherence in sampling different geographic areas. By using exactly the same number of profiles collocated within 1°, we ensure the same coverage and sampling by both lidars.~~ 5). If the detection efficiency of different cloud types were the same for two instruments, the ~~plots~~pairs of Fig. 5 panels (a;f), (b;g), (c;h), (d;i), and (e;j) would have been close to each other because of two reasons. First, the horizontal variability of clouds would ~~cancel~~have canceled out due to averaging over ~~a large number of~~ many profiles within the zone ~~and~~. Second, the diurnal variation is ~~small~~minor over oceans, which ~~constitute~~make up two thirds of the ~~cases~~data used ~~to build~~for Fig. ~~4 (Noel~~ 5 (Noël et al., 2018; Chepfer et al., 2019; Feofilov and Stubenrauch, 2019). Analyzing the Fig. ~~4~~,5 one can note ~~the following~~: (1) the SR~~/altitude~~-height histograms of CALIOP (Fig. ~~4a~~5c-e) ~~are characterized by~~show two distinct peaks corresponding to low-level and high-level clouds; this feature is coherent with other observations, e.g. with GEWEX (Global Energy and Water cycle Experiment) cloud assessment (Stubenrauch et al., 2013); (2) the SR~~/altitude~~-height histograms built for ~~SRs~~ $SR'(532nm, z)$ retrieved from ALADIN's observations (Fig. ~~4f~~ 5f-j) are characterized by a smoother occurrence frequency plot where the two-peak structure is less pronounced than ~~for~~in CALIOP; (3) even though ALADIN detects ~~some~~polar stratospheric clouds ~~in polar stratosphere~~ (PSCs), its overall sensitivity to ~~high~~ clouds ~~(>7~~above ~3 km~~)~~ altitude is lower than that of CALIOP; (4) both rows show ~~certain consistency of zone-to-zone change~~a good agreement up to ~3km altitude ~~while~~ ; (5) both datasets show a layer of enhanced backscatter closer to the ~~behavior above requires a more detailed view. We would like~~tropopause, which is not strong enough to ~~stress here that no linear scaling applied uniformly to SRs at all heights could change~~trigger the ~~ratio of high~~ cloud detection ~~frequency to low cloud detection frequency of ALADIN. The same is true for CALIOP~~defined in this work. In the next step, we compare the "instantaneous" profiles provided by CALIOP and ALADIN having in mind the ~~peculiarities of~~ cloud detection sensitivity ~~differences~~issues observed in Fig. 4~~5~~.

~~3~~5.2 Comparing ~~pseudo~~ individual SR profiles ~~at ALADIN's L2A product resolution~~

~~To address~~Since Fig. 5 revealed certain differences between the ~~high cloud detection sensitivity~~two datasets, we ~~have~~ inspected ~~the 6h nighttime subset of~~ collocated data~~,~~ looking for the specific cases, which would explain the averages shown in Fig. 5. First, we wanted to test the ALADIN's capabilities of high cloud detection. The subset we used for this task had to

satisfy the following criteria: (1) both instruments should have at least one strong SR peak; (2) the ~~vertical position~~height of this peak detected by one instrument should match ~~that~~the height of the peak detected by a second instrument within 1 km; (3) the CALIOP SR profile should have a ~~secondary~~ peak at or above 9 km (Fig. ~~5a~~6a-j). For the comparison purposes, the panels in Fig. ~~5~~6 represent the individual profiles belonging to the same 5 zones as the panels of Fig. ~~4. For the sake of simplicity, we compare the $SR_{355}(z)$ profiles recalculated to $SR_{532}(z)$, but we also show the source $SR_{355}(z)$ profiles for reference purposes. Regarding the conversion using Eq. 1, the strong peaks selected this way demonstrate a qualitative agreement between the peak values calculated from SR_{355} and peak retrieved SR_{532} values. In Appendix A, we demonstrate the correlation between individual pairs of CALIOP and ALADIN SR profiles; the conclusion of this exercise is that it justifies using Eq. 1, but the uncertainties of the analysis do not allow to refine the conversion coefficients.~~ 6. As for the potential capability of ALADIN to detect high clouds, the subset shown in Fig. ~~5a~~6a-e represents the cases~~,~~ for which ~~the~~this instrument ~~was capable of retrieving~~retrieved the peak of about the same magnitude and height as the peak detected by CALIOP. Even though these cases exist, they are ~~far~~ less frequent than those shown in Fig. ~~5f~~6f-j. ~~We~~ when ALADIN misses a high cloud, but detects a lower cloud reported by CALIOP.

To test whether the said mismatch is linked with the diurnal variation, we varied Δtime in 3−12h limits, but this did not ~~detect and correlation between the collocation criteria (Δdist; Δtime) and~~ change the frequency of occurrence of ~~these cases, it's just a statistical observation that both types of cases exist and the former are less frequent than the latter.~~high and low cloud detection. This ~~observation~~ gives a hint that the instrumental part itself provides the backscatter information sufficient for ~~some~~ cloud detection up to 20 km, but the detection algorithm suppresses noisy solutions. The reasons for this presumable "noise" might be linked with instrumental issues discussed below, but they might be also related to the ratio of particulate and molecular backscatter at 355 nm. Let's have a closer look: the molecular signal is stronger at 355nm and the particulate signal is comparable to that at 532 nm. At the same time, ALADIN is an HSRL instrument, and the separation to molecular and particulate component requires disentangling of the signals measured in Mie and Rayleigh channels (cross-talk correction). Correspondingly, the error propagation in this procedure might adversely affect the SNR in Mie channel and, therefore, the SNRs of the extinction, backscatter, and recalculated $SR'(532nm, z)$. The PSC detection discussed below (see also Fig. ~~4f~~ 5f) confirms this assumption because the vertical extent and the composition of these clouds yield a ~~strong signal. Further speculations on this subject are beyond the scope of the present article~~stronger SR signal than that for the cirrus clouds (Noël et al., 2008). Characterizing these differences and their impacts on retrieved clouds is beyond this study and it requires further investigation, but we believe that the high cloud detection agreement might be improved by studying the collocated cases provided in the supplementary materials and by applying different noise filtering techniques in the L0→L1→L2 elements of the ALADIN retrieval chain. ~~Figures~~ As for the Fig. 5k-o, we will ~~be discussed~~discuss them below in the context of low-level cloud observations.

~~3~~5.3 Cloud detection agreement

In Fig. 7, we show zonal cloud fraction profiles built from the collocated dataset of $SR(532nm, z)$ and $SR'(532nm, z)$ by applying the threshold (Eq. 8) uniformly to both datasets. Despite the differences in SR absolute values, the $CF(z)$ profiles estimated from CALIOP and ALADIN agree relatively well. The Pearson's correlation coefficient for the panels in Fig. 7a,b varies between 0.7 and 0.9 for most heights (Fig. 7c) and the relative difference between the panels changes from 50% in the lower layers through minus 50% at 11km and to 25% near tropopause (Fig. 7c).

To illustrate the ~~peculiarities of zonal and altitudinal behavior of cloud detection~~ zonal $CF(lat, z)$ profiles agreement ~~between two considered instruments, we have~~, we split the collocated data into four groups ~~(Fig. 6). For each altitude/latitude grid point, we have estimated the number of cases when both instruments have detected a cloud ($SR_{532}(z) > 5$), when neither of instruments has detected a cloud, when only CALIOP has detected a cloud, and when only ALADIN has detected a cloud. For the sake of simplicity, we will call them YES_YES, NO_NO, YES_NO, and NO_YES cases. It is clear~~defined in Section 3.5 (Eq. 11 and text preceding it). We show the corresponding distributions of $R_{YES\_YES}(lat, z)$, $R_{NO\_NO}(lat, z)$, $R_{YES\_NO}(lat, z)$, and $R_{NO\_YES}(lat, z)$ in (Fig. 8). From the definition (Eq. 11), it follows that in the case of an ideal ~~experiment~~agreement, the ~~number of~~ mismatched ~~cases (YES_NO~~case rates, $R_{YES\_NO}(lat, z)$ and ~~NO_YES)~~ $R_{NO\_YES}(lat, z)$ should ~~tend~~be equal to zero. However, Fig. 8c and Fig. 8d show occurrence frequencies comparable to and sometimes even exceeding those of Fig. 8a. From the study presented in Section 4.2.~~4~~, we expect that the ratio of ~~(YES_YES+NO_NO)/(YES_YES+NO_NO+YES_NO+NO_YES)~~$R_{YES\_YES}(lat, z)$ to $CF(lat, z)$ should be about 0.~~77~~81±0.~~17~~07 if ~~both instruments detect~~we assume that CALIOP can be used as a reference for cloud detection sensitivity. If we plot the ~~clouds with the same efficiency. In~~$CDA_{norm}(z)$ estimated from Fig. ~~6a~~8a and Fig. 7 (Eq. 12), we ~~show~~will see that it fits the ~~ratio of YES_YES cases~~prescribed value up to ~~the total number of collocated profiles per~~~3km. Above this altitude~~/latitude bin. This panels~~, the normalized cloud detection agreement oscillates around 0.5 (cyan curve in Fig. 4).

The distribution of $R_{YES\_YES}(lat, z)$ (or $CDA(lat, z)$) shown in Fig. 8a resembles a typical cloud ~~amount~~fraction profile plot~~, and this~~ (compare with Fig. 7). This is ~~expected~~not surprising because ~~in the case of an ideal agreement the aforementioned ratio is equivalent to cloud amount definition. Below, we will also discuss the YES_YES statistics normalized to cloud amount, but at this point we also want to study the other cases, which cannot be normalized this way.~~of $R_{YES\_YES}(z)$ must turn to $CF(z)$ if the agreement is perfect (see Eqs. 10, 12). Even though the distribution in Fig. ~~6a looks physical, the absolute numbers are somewhat low and this is explained by YES_NO and NO_YES distributions (Fig. 6c and d, respectively). As for NO_NO agreement (Fig. 6b),~~8a looks physical, the ratios for the heights above 3km are ~40% lower than expected from the theoretical estimates. As one can see from Fig. 8c, the missing cases also form a structure, which resembles $CF(lat, z)$ distribution. This shows that 40% of ALADIN's $SR'(532nm, z)$ values are below the threshold (Eq. 9). Technically, this could be fixed by lowering the detection threshold, but this would increase the $R_{NO\_YES}(lat, z)$ occurrence frequency (Fig. 8d) that is not desired.

As for $R_{NO\_NO}(lat, z)$ shown in Fig. 8b, it is close to 100% in the high-altitude area where there are no clouds. This indicates that the noise-induced false detection rate of both instruments is low~~, and this~~ that is a good ~~sign~~result.

~~If we consider the mismatch of YES_NO type (Fig. 6c), we will see that the altitudinal/zonal distribution of the mismatch occurrence frequency resembles that of the YES_YES type. A part of mismatch can be explained by theoretically allowed cloud detection disagreement discussed in Section 2.4. However, the occurrence frequency of YES_NO cases above 3 km is roughly twice that of YES_YES cases, and this indicates the retrieval sensitivity issue of ALADIN. The NO_YES mismatches (Fig. 6d) require specific attention because they are not expected from the methodological point of view: the cloud~~We draw the readers' attention to the fact that the NO_YES mismatches, the occurrence frequency $R_{NO\_YES}(lat, z)$ of which is high near ~2km (Fig. 8d), are not expected for the considered combination of lidars. Let us explain. The molecular extinction at 355 nm is larger than at 532 nm and the observation geometry of ALADIN makes the optical paths *1 / cos(~~SVA~~35°) = 1.22* times longer than those for CALIOP, where ~~SVA stands for~~ 35° is a satellite viewing angle ~~of 35°~~. At the same time, the particulate backscatter coefficients at these wavelengths are almost the same. Therefore, for the same low-level cloud, all other factors being equal, cloud detection should be easier for CALIOP and not for ALADIN. The typical individual profiles corresponding to NO_YES mismatches are shown in Fig. 5k-o. As one can see, despite the unfavorable observation conditions (e.q. ~~an opaque~~a cloud with peak $~~SR_{532}~~SR(532nm)$ value of ~~22~~20 at ~~9~~7 km in Fig. ~~5~~6l), ALADIN ~~reports~~retrieves one or two valid points beneath ~~the~~a cloud ~~whereas it does not report anything at 9 km height where CALIOP sees a thick cloud. These cases do need our special attention.~~ detected by both instruments. Let us consider possible reasons for the observed behavior:

(1) ~~On the one hand,~~Since many cases of ~~this~~NO_YES type are over the ocean, ~~so~~ one can rule out the continent surface echo ~~mixed with~~admixture to atmospheric backscatter ~~and treated like an atmospheric signal. On the other hand, the NO_YES cases are often accompanied by the structures similar to those presented in Fig. 5k,l,n which are probably provoked by a presence of a cloud at these heights. The perturbations~~signal.

(2) The horizontal cloud inhomogeneity could explain the individual cases shown in Fig. 6k-o, but it cannot explain the general behavior observed in Fig. 8d.

(3) The higher detection rate in the lower layers cannot be fixed by increasing the SR threshold (Eq. 8) because it will adversely affect the agreement at other altitudes.

(4) Since the $SR'(532nm, z)$ values in this work were recalculated from the source ALADIN data at 355 nm, the uncertainties and biases of the parameters used for recalculation (Section 3.4) could have biased the results. These effects will accumulate along the line of sight, so the errors should be larger near the ground.

Let us verify the last hypothesis and consider the elements of Eq. 1:

(4a) $\alpha_{part}(\lambda, z)$ and $\beta_{part}(\lambda, z)$ are provided by ALADIN and their uncertainty or bias will propagate through the calculations. Moreover, a small bias in $\alpha_{part}(\lambda, z)$ will accumulate with distance (Eq. 1). Therefore, one cannot

rule out this source of discrepancy. To explain the observed behavior, one needs to ~~the extinction and backscatter~~ have either smaller $\alpha_{part}(\lambda, z)$ values, or larger $\beta_{part}(\lambda, z)$ values, or both.

(4b) $\alpha_{mol}(\lambda, z)$ and $\beta_{mol}(\lambda, z)$ are calculated with high accuracy given that the molecular density profile ~~caused by these structures might propagate downwards, thus causing the appearance of the false peaks in the lower layers of ALADIN's data. This indicates a need for a quality flag refinement~~in CALIOP comes from the GEOS-5 DAS database, see (Rienecker, 2008). The uncertainties of the parameters used for their estimate are small (Bucholz, 1995; Ciddor, 1996), so they cannot give preference to the low-level clouds and suppress the higher ones. Therefore, it is unlikely that these parameters are responsible for NO_YES cases.

(4c) The physical meaning of the multiple scattering coefficient η is an increase in number of photons remaining in the lidar receiver field of view (Garnier et al., 2015). Its value depends on type of scattering media and varies between 0.5 and 0.8 (Chiriaco et al., 2006; Chepfer et al., 2008, 2013; Garnier et al., 2015). Theoretically, this uncertainty could affect our estimates of $ATB(\lambda, z)$. To reduce the low-level clouds in Eq. 1, one needs to increase η. If we take the maximal physically allowed value of 1 for this coefficient, we reduce the fraction of NO_YES cases in the lower layers ~~in the presence of a thick cloud above and the improvement of thick cloud detection itself. Apparently, the CALIOP cloud retrievals beneath thick clouds do not suffer from these effects.~~

~~To test whether the aforementioned disagreements are at least partially caused by the cloud definition and SR recalculation to another wavelength and whether the agreement could be improved, we varied the SR threshold for ALADIN, assuming the ±50% uncertainty on the parameters forming the coefficients of Eq. 1. However, this exercise yielded no optimum value for SR threshold: its lowering for ALADIN increased the number of YES_YES and reduced~~by a factor of ~2, but we will worsen the YES_YES agreement at the same heights and increase the number of YES_NO cases~~, but at the same time it increased the frequency of NO_YES cases. Correspondingly, increasing the threshold reduced the number of NO_YES cases, but it adversely affected the YES_YES agreement.~~ because of the decreased transparency in the exponent of Eq. 1. Still, this parameter remains on the list of the variables, which may affect the quality of the $SR'(532nm, z)$ conversion.

Summarizing this ~~comparison, one can~~ section, we conclude that (a) a cloud layer detected by CALIOP is detected by ALADIN in ~~50~~80% of cases for ~~clouds~~cloud layers below ~3km and in ~~30~~50% of cases for higher ~~clouds~~cloud layers; (b) in the cloud-free area, the agreement between the datasets is good that ~~indicates~~shows a low frequency of false positive detections by both instruments; (c) ~~one~~ half of the cases when ALADIN detects a low-level cloud missed by CALIOP ~~should be attributed to false positive detection of the low cloud in the presence of a higher opaque cloud, which perturbs the retrieval in the lower layers.~~ is unlikely caused by sampling and geometrical differences, diurnal variation, or uncertainties in the $SR'(532nm, z)$ profile recalculation.

35.4 Cloud altitude detection sensitivity

Besides marking the profile elements as "cloudy" and "not cloudy" and comparing the cloud We now analyze if clouds detected by the two lidars peak at the same altitude. We note that we are not looking for an altitude offset here. The altitude detection of both instruments is beyond question. Instead, we would like to check whether the higher detection statistics as we did in the previous section, it would be interesting to obtain cloud peak detection statistics for pairs of collocated profiles like those shown in Fig. 5. This exercise is not aimed at revealing any altitude offset in backscatter signal registration, because this part of experimental setup is robust in both instruments. But, as we saw in Fig. 4 and Fig. 6, the sensitivity of ALADIN to high rate of lower clouds is lower than to lower clouds and a convolution of sensitivity curve with the backscatter profile can skew the cloud peak position and the average cloud height. To illustrate this effectleads to slight systematic differences in the cloud altitudes derived from the 2 lidars. To do so, we have carried out the following analysis. For each pair of collocated profiles selected for YES_YES plot (Fig. 6a 8a), we scanned vertically through ALADIN profile step by step, looking for a local maximum, which we define as a set ofsatisfying the following conditions:

$$SR(i) > SR_{threshold}; 5;\ \mathrm{SR(i)} > \mathrm{SR(i-1)};\ SR(i) > SR(i+1) \qquad (2(10)$$

Mis en forme : Droite

where $SR_{threshold}$ is the cloud detection threshold at 532 nm, which is equal to 5. For each local peak found, we have searched for a peak or for a maximal value of CALIOP's SR(z) profile in the vertical vicinity of ±3 km from the peak height determined from ALADIN. The choice of a "reference" dataset in this case depends on the detection probability, and if one choses CALIOP as a reference, the distance to the nearest ALADIN peak might be spoiled by lower probability of cloud detection by ALADIN and the distribution will be skewed. The We have chosen theses search limits are arbitrary and they have been chosen fromby inspecting the collocated profiles taking into account , considering the natural variability of cloud heights at distances of about 100 km, estimated from thesimilar to those used in collocations. According to our analysis of CALIOP data used in this study (~, at these distances ~75% of clouds move vertically by less than 1 km, ~8% by 1−2 km, ~5% by 2−3km, ~4% by 3−4km, ~3% by 4−5 km and ~5% by more than 5 km). The. We note that by imposing the ±3 km search criteria, we filter out about 12% of the cases linked to natural variability that slightly reduces the number of cases selected for the analysis. At the same time, we lower the rate of picking up the peak from a different cloud layer.

We stored the differences between the ALADIN's and CALIOP's cloud peak heights have been stored and then averaged them in the corresponding latitude/altitude bins (Fig. 78). As one can see, the cloud height detection agreement is better than 0.2 km below ~3 km and, surprisingly, for some of high-altitude zones. For good for the tropical zone, this high clouds. This is probably linked with thick Ci clouds, which should be reliably detected by both instruments. For the Southern polar zone, this figure reveals the PSCs, which are barely visible in Fig. 6a8a, but which can be seen in Fig. 4f5f for ALADIN. These clouds form at very low temperatures and are partially composed of large ice particles yielding a reflection, which is reliably detected at both wavelengths if the layer is thick enough (e.g. Adriani et al., 2004; Noël et al., 2008; Snels et al., 2021). However, about 50% of PSCs contain water droplets composed of super-cooled ternary solutions (STS), which are smaller. The backscatter of these droplets at 355 nm is roughly twice as large as that of 532 nm (Jumelet et al., 2009), so these clouds

may appear brighter in our $SR'(532nm, z)$ representation. This explains the PSC zone behavior in Fig. 5a,f, Fig. 7b, and Fig. 9.

As one can see in Fig. 9, the higher sensitivity to low-level clouds shifts the average ALADIN's cloud height downwards compared to CALIOP. At the heights of 3−5 km, the shift is as large as 0.8−1.4 km. One can attribute a part of this effect to the reasons discussed for the ~~clouds between ~3~~existence of NO_YES cases (e.g. if one assumes larger values of η, the average downward shift will be smaller, but this kind of "tweaking" would need to be justified). Summarizing, the assumption of skewing the average cloud height through higher sensitivity to lower clouds proves to be valid, and we estimate a mean downward shift to be equal to 0.5±0.6 km ~~and ~10 km height, the height sensitivity effects skew the effective cloud height detected by ALADIN downwards by 0.5−1.0 km. This is coherent with Fig. 4, which shows lower frequency of occurrence of high clouds detected by ALADIN. At least a part of the cloud peak shifts in the 3−5 km layer should be attributed to the reasons discussed for NO_YES statistics and these differences should reduce when the aforementioned quality flags for cloud-perturbed retrievals are fixed.~~ .

~~3~~5.5 Temporal evolution of cloud detection agreement

As it was mentioned in Section 2.1, the ALADIN lidar faced several technical issues, which hindered getting the planned specifications. Among them, we named the "hot pixels" issue, which requires some explanation. First, the information from them is not completely lost, and there is a way of recalibrating of these pixels (Weiler et al., 2021). Second, if we compare the hot pixels distribution for Mie and Rayleigh channel ACCD detectors for the period considered in this work (see Table 2 of Weiler et al., 2021), we will see 3 and 5 new hot pixels for Mie and Rayleigh matrices, respectively. ~~ALADIN is a relatively young instrument, and its calibration/validation activity is still on the way (Baars et al., 2020; Donovan et al., 2020; Kanitz et al., 2020; Reitebuch et al., 2020; Straume et al., 2020). This includes, but is not limited to internal calibration and comparisons with other observations. The Aeolus mission faced a number of technical issues, which hindered obtaining the planned specifications. These issues are related to several factors: (a) laser power degradation (60 mJ/pulse instead of 80 mJ/pulse) and signal losses in the emission and reception paths (33%) that results in lower signal to noise ratio (SNR) than planned, (b) telescope mirror temperature effects biasing the wind detection and calibration of Mie and Rayleigh channels of ALADIN, (c) constantly increasing number of hot pixels of both ACCD detectors (Weiler et al., 2021) leading to errors both in wind speed and in retrieved optical parameters of the atmosphere (the number of hot pixels increased by a factor of 1.4 during the period considered in this work). The Aeolus teams managed to mitigate some of these adverse effects (e.g. Baars et ql., 2020; Weiler et al., 2021), and it would be interesting to see whether the pilot L2A dataset, Prototype_v3.10 is free of cloud detection quality trends. If true, this would indicate a good calibration and consistent processing of Level 0 through Level 1 to Level 2A.~~

For Mie detector matrix, the lowermost hot pixel, which appeared during the considered period, corresponds to ~15 km height. Even though these pixels do not overlap with the maxima of cloud height distributions, they still might affect the retrieval results below because of the optical path passing through the corresponding layers (see Eq. 1). As for new Rayleigh

hot pixels, the lowermost two correspond to 1 km height, the next two – to 5 km, and the last one – to 18 km. The Rayleigh matrix pixels are not directly linked to cloud detection, but their cross-talks are used in ALADIN's $\alpha_{part}(\lambda, z)$ and $\beta_{part}(\lambda, z)$ calculations, so they might also affect the results.

In Fig. ~~8 and 9~~10a-d, we show the temporal evolution of ~~cloud detection agreement per height bins. The panels of Fig. 8 are consistent with those of Fig.~~ $R_{YES\_YES}(time, z)$, $R_{NO\_NO}(time, z)$, $R_{YES\_NO}(time, z)$, and $R_{NO\_YES}(time, z)$ over the whole period of collocated data set (28/06/2019−31/12/2019). Figure 10e and Fig. 10f show the temporal evolution of $CDA_{norm}(time, z)$ in two forms: as a color plot and as 2D linear fitting at the heights characterized by high occurrence frequency (0.75 km, 2.25 km, 6 ~~whereas Fig. 9 considers only the evolution of YES_YES statistics, which corresponds to Fig. 6a and Fig. 8a, normalized by cloud amount.~~.25 km, 8.75 km, and 10.0 km). Unfortunately, the period available for analysis does not cover the ~~whole~~entire year, so the plots Fig. 10a-d can be affected by seasonal variation of cloud distributions. Still, the latitudinal and longitudinal coverage of collocated data does not change throughout the year and a mixture of Northern and Southern hemispheres should partially compensate for seasonal anomalies. ~~The signatures one~~As for the $CDA^{obs}_{norm}(time, z)$ panels (Fig. 10e,f), the normalizing by $CF(time, z)$ should ~~be looking for are experimental~~compensate for the seasonal variation in these plots. Possible artefacts linked ~~with~~to laser power degradation, hot pixels ~~appearance~~, and bias ~~corrections. If these issues are not properly compensated, the "agreement panels" (Fig. 8a,b) should demonstrate~~correction would likely show up as a decrease in $R_{YES\_YES}(time, z)$ and $R_{NO\_NO}(time, z)$ occurrence ~~frequency with time and the~~frequencies (Fig. 10a,b) and as an increase in $R_{YES\_NO}(time, z)$ and $R_{NO\_YES}(time, z)$ occurrence ~~frequency in "disagreement panels" (Fig. 8c,d) should increase with time. As one can see~~frequencies (Fig. 10c,d).

However, this is not the case: visually, all ~~4~~ panels of Fig. ~~8~~10a-d do not show any anomaly, which would go beyond their noise levels ~~(~~. We note that there is a special region corresponding to a forced vertical bin size reduction in the period of 28/10/2019−10/11/2019, which is marked by white dashed lines in Fig. ~~8~~10 and which should not be considered at heights below 2250m~~).~~. To quantify the tendencies and to compare them with noise levels, we ~~have normalized~~ analyzed the $CDA^{obs}_{norm}(time, z)$ distributions (Fig. ~~8a (YES_YES cases) by cloud amount per altitude/time bin. This procedure helps to get rid of seasonal variation of clouds.~~10e,f). The results presented in ~~Fig. 9~~these panels confirm the previous conclusions regarding the ~~altitude distribution of cloud detection agreement~~$CDA^{obs}_{norm}(z)$ profile: for the clouds below 3 km, it is better than for higher ones (~~61±16%~~68±12% at 0.75 km and ~~34±18% for 0.75 and~~55±14% at 2.25 km~~, respectively~~ versus ~~24±10%, 26±10~~34±14%, ~~39±13~~%, and ~~22±12% for~~42±14% at 6.75 km, 8.75 km, and 10.25 km, respectively. ~~As for the tendencies, the low-level clouds demonstrate an improvement towards the end of the year whereas the agreement for 6.75 km and 10.25 km becomes slightly worse by the end of the considered period~~The uncertainty limits in these estimates are relatively large. Nevertheless, the absence of statistically significant trends indicates that the compensation for hot pixels effects (Weiler et al., 2021) and for signal losses in the emission and reception paths removes the signatures of the experimental issues from the ALADIN L2 optical products at least down to these uncertainty limits.

Mis en forme : Couleur de police : Texte 1

If we compare the hot pixels distribution for Mie and Rayleigh channel ACCD detectors at the beginning and at the end of the time scale of Fig. 8 and 9 (Table 2 of Weiler et al., 2021), we will see 3 and 5 new hot pixels for Mie and Rayleigh matrices, respectively. Even though the Rayleigh matrix pixels are not directly linked to cloud detection, their information is used for the ALADIN SR calculations. For Mie matrix, the lowermost hot pixel, which appeared during the considered period, corresponds to ~15 km height and this cannot affect the tendencies shown in Fig. 9. As for new Rayleigh hot pixels, the lowermost two corresponds to 1 km height, the next two – to 5 km height, and the last one – to 18 km. This information does not explain the observed behavior, either. Overall, considering relatively large error bars for all five altitudinal sections presented in Fig. 9b and the variety of the observed slopes, one cannot make a sound conclusion neither regarding the deterioration (or the improvement) of cloud detection agreement nor regarding the link between hot pixels appearance and change of cloud detection quality. A proper conclusion is that one does not detect the tendencies beyond the variability limits of the analyzed parameter and that the hot pixels appearance cannot be tracked from the cloud agreement plot, indicating that compensation for hot pixels effects (Weiler et al., 2021) works properly within the discussed uncertainty limits. The same can be said regarding the other known technical issues: the signal losses in the emission and reception paths do not transform into a clear signature in cloud detection agreement plots. Moreover, they should have affected the detection of low and high clouds in the same way that is not observed in Fig. 8 and 9.

46. Conclusions

The active sounders are advantageous for atmospheric and climate studies because they provide atmospheric parameters at altitudeprecise vertically resolved scale with high accuracy.information. For continuity of climate studies and monitoring the globalcloud changes, it is essential to understand the differences between spacebornespace-borne lidars operating at different wavelengths, flying aton different orbits, and utilizingusing different observation geometries, receiving paths, and detectors. In this article, we addressed an intercomparison ofcompared the ALADIN and CALIOP lidars using their scattering ratio products (CALIPSO-GOCCP and Aeolus L2A, Prototype_v3.10) for the period offfrom 28/06/2019– to 31/12/2019.

Using the COSP2 lidar simulator coupled with output from the EAMv1 model and a horizontal cloud variability parameterization, we estimated a theoretically achievable agreement in cloud detection of 0.77±0.17 for these two instruments with their orbits, averaging, and observation geometry.

On the one hand,We defined the spatial collocation criterion of 1° chosen in this work is based on the averaging distance of Aeolus L2A Prototype_v3.10 data. On the other hand, theThe temporal collocation criterion of Δtime < 6h used in this work is a tradeoff between the geographical coverage of the collocated profiles, their number, and uniformity of Δtime distribution throughout the globe. With the named criteria, we managed to findfound ~7.8E4 collocated nighttime profiles, which underwent a series of analysis summarized here. For the simplicity of the comparison with CALIOP, we converted SR_{355} of ALADIN to SR_{532} and we discuss the sensitivity of the results to the conversion parameters.

~~Overall,~~For an adequate comparison with the ~~SR product~~CALIOP's $SR(532nm, z)$, we converted ALADIN's $\alpha_{part}(355nm, z)$, $\beta_{part}(355nm, z)$, and $SR^{A}(355nm, z)$ to $SR'(532nm, z)$ and we discussed the uncertainties of this conversion.

Before analyzing the actual observations, we performed a numerical experiment to estimate the best achievable cloud detection agreement between the two missions. We found that the agreement between ALADIN ~~is characterized by lower sensitivity to high~~ and CALIOP clouds ~~above ~7~~should be about 0.81±0.07 regardless of the altitude. The numerical experiment used the outputs from a global atmospheric model coupled with a lidar simulator, a horizontal cloud variability parameterization, and considering the lidar orbit, sampling, averaging, noise, and observation geometry differences in the two lidars.

Analyzing the actual observations, namely, the ALADIN dataset converted to $SR'(532nm, z)$ profiles and compared with the $SR(532nm, z)$ profiles of CALIOP, we report a good agreement in the lower atmospheric layers. Above 3 km ~~than CALIOP, that we~~, the agreement is worse. We explain this by lower SNR for ALADIN at these heights that is due both to physical reasons (~~smaller~~ ratio of particulate to molecular backscatter is smaller at 355 nm than at 532 nm) and technical reasons (~~hot pixels,~~ lower emission and lower transmissivity of receive path than planned). ~~Large sensitivity to~~ This hypothesis is confirmed by PSCs, the backscatter from which is stronger at 355 nm than at 532 nm, leading to high SNR and reliable retrieval in this zone for ALADIN.

Switching from the absolute $SR(532nm, z)$ and $SR'(532nm, z)$ values to cloud fraction profiles obtained by applying a fixed cloud detection threshold of $SR > 5$, the zonal mean cloud profiles of the two compared instruments show relatively good agreement, with Pearson's correlation coefficient varying from 0.7 to 0.9 and relative difference varying within ±50% on the altitude. In the lower 3 km, the estimated $CDA_{norm}^{obs}(z)$ profile almost reaches its theoretically estimated value CDA_{norm}^{theor} of 0.81±0.07 whereas in the upper layers, its value is about 40% less. Better detection of lower clouds ~~leads to prioritizing the lower cloud solutions to higher ones in the case of a continuous cloud or a double layer. This~~ skews the mean ALADIN's cloud peak height in pairs of ALADIN/CALIOP profiles by ~0.5±0.~~4~~6 km downwards. ~~Interestingly~~For the reasons explained above, the agreement of PSC peak heights and of tropical high clouds does not suffer from these effects. ~~We explain this by large vertical extent and composition of PSCs, which make them a better target for ALADIN than the tropospheric clouds. In the~~ In the cloud-free area, the agreement between two instruments is good, indicating a low rate of noise-induced false detection for both instruments.

Last, but not least, the temporal evolution of cloud agreement does not reveal any statistically significant change during the considered period. This ~~indicates~~shows that hot pixels and laser energy and receiving path degradation effects in ALADIN have been mitigated at least down to the uncertainties of the following normalized cloud detection agreement values: ~~61±16~~68±12%, 55±14%, 34~~±18%, 24±10%, 26±10~~14%, 39±13%, and ~~22±12~~42±14% estimated at 0.75 km, 2.25 km, 6.75 km, 8.75 km, and 10.25 km, respectively. We believe that the provided collocated dataset will facilitate the further analysis and improvement of ALADIN L2A data. From our point of view, the outlook for a cloud product retrieved from

Mis en forme : Couleur de police : Texte 1

Mis en forme : Couleur de police : Texte 1

Mis en forme : Couleur de police : Texte 1

Mis en forme : Couleur de police : Texte 1

Mis en forme : Couleur de police : Texte 1

ALADIN observations to be part of cloud lidar long record is promising: its L1 to L2 algorithms and the thresholds can be adapted to retrieve the same clouds as from CALIOP. This will help to better understand the instrumental and observational differences and build a long-term cloud climate record.

Appendix A

The analysis of the collocated data may enable the researcher not only to validate one dataset against another one, but also to validate a physical concept or to retrieve an important model parameter (e.g. Holl et al., 2010; Feofilov and Petelina, 2010; Feofilov et al., 2012; Virtanen et al., 2018). In this section, we report the results of a validation attempt aimed at the retrieval of the scaling coefficients used in Eq. 1 and through them the model assumptions. To do this, we searched the collocated database for the events which would satisfy the following criteria: (a) the ALADIN SR profile should contain at least one valid point with the corresponding quality flags (see Section 2.2) and with SR higher than halved $SR_{threshold}$; (b) the profiles should fit the selection criteria used for cloud altitude detection sensitivity (Section 3.4); (c) the CALIOP peak should contain more than one point to avoid sampling problems. For these profiles, we picked up not only the major peak values, but also the secondary peak values if the vertical agreement of the profiles was good like in Fig. 5a,c,d,e. The corresponding pairs of SR_{CALIOP} and $SR_{ALADIN355}$ values have been binned using the 0.2 × 0.07 SR bins, which reflect the differences between SR_{532} and SR_{355}. The corresponding frequency occurrence distribution for this dataset is shown in Fig. A1. Even though the SR pairs exist for opaque domain, the spread increases and the values beyond $SR_{532} = 10$ are neither informative nor suitable for the maximal probability search algorithm (see Dawkins et al., 2018) used for the analysis. Like in Fig. 11 of (Dawkins et al., 2018), the red dots in Fig. A1 represent the centers of Gaussian fit to perpendicular transects. White dashed line shows a linear fit to the dataset represented by these red dots, and the corresponding conversion if given by the following equation:

$$SR_{532} = SR_{355} \times (3.8 \pm 1.0) - (3.3 \pm 1.4) \quad \text{(A1)}$$

Even though the coefficients in Eq. A1 differ from those of Eq. 1, the black dashed line in Fig. A1 representing Eq. 1 does not significantly deviate from the white dashed line representing Eq. A1 and both lines fit the maximum probability plot within its uncertainty limits. We conclude that the collocated dataset proves the basic equations used to derive Eq. 1 though its uncertainties do not allow to retrieve the corresponding fitting parameter A of (Collis and Russell, 1976) from such a comparison.

Data availability

The collocated dataset used in this work can be downloaded from ResearchGate repository using the following link https://doi.org/10.13140/RG.2.2.~~11237.12009~~16562.94409 (Feofilov et al., 2021~~).~~)

Author contribution

HC, VN, MC, and AF: conceptualization, investigation, methodology, and validation; RG, CG, and AF: data curation and formal analysis; AF: writing original draft; AF and HC: review and editing.

Competing interests

The authors declare that they have no conflict of interest.

Disclaimer

The presented work includes preliminary data (not fully calibrated/validated and not yet publicly released) of the Aeolus mission that is part of the European Space Agency (ESA) Earth Explorer Program. This includes aerosol and cloud products, which have not yet been publicly released. ~~Aerosol and cloud products will become publicly available by spring 2021.~~ The processor development, improvement and product reprocessing preparation are performed by the Aeolus DISC (Data, Innovation and Science Cluster), which involves DLR, DoRIT, ECMWF, KNMI, CNRS, S&T, ABB and Serco, in close cooperation with the Aeolus PDGS (Payload Data Ground Segment).

Acknowledgements

This work is supported by the Centre National de la Recherche Scientifique (CNRS) and by the Centre National d'Etudes Spatiales (CNES) through the Expecting Earth-Care, Learning from A-Train (EECLAT) project. The processor development, improvement and product reprocessing preparation are performed by the Aeolus DISC (Data, Innovation and Science Cluster), which involves DLR, DoRIT, ECMWF, KNMI, CNRS, S&T, ABB and Serco, in close cooperation with the Aeolus PDGS (Payload Data Ground Segment). ~~The authors want to thank P. L. Ma (PNNL) for providing the outputs of the EAMv1 atmospheric model and F.~~P.-L. M. acknowledges supports from the U.S. Department of Energy, Office of Science, Office of Biological and Environmental Research, Regional and Global Model Analysis (RGMA) program area. The authors want to thank F. Ehlers (EOP-SMA/ESTEC/ESA), A. Straume (ESTEC/ESA), and O. Reiterbuch (DLR) for their comments on the preliminary version of the manuscript.

References

ADM-Aeolus Science Report, SP-1311, ISBN 978-92-9221-404-3, ISSN 0379-6566, Coordinated by: P. Ingmann, Mission Science Division, Atmospheric Unit, Published by: ESA Communication Production Office, The Netherlands, 121pp, 2008.

Adriani, A., Massoli, P., Di Donfrancesco, G., Cairo, F., Moriconi, M. L., Snels M.: Climatology of polar stratospheric clouds basedon lidar observations from 1993 to 2001 over McMurdo Station,Antarctica, J. Geophys. Res., 109, D24211, doi:10.1029/2004JD004800, 2004.

Ansmann, A., Wandinger, U., Le Rille, O., Lajas, D., and Straume, A. G.: Particle backscatter and extinction profiling with the ~~spaceborne~~space-borne high-spectral-resolution Doppler lidar ALADIN: methodology and simulations. Appl. Optics, 46 (26), 6606-6622, doi:10.1364/AO.46.006606, 2007.

Baars, H., Geiß, A., Wandinger, U., Herzog, A., Engelmann, R., Bühl, J., Radenz, M., Seifert, P., Ansmann, A., Martin, A., Leinweber, R., Lehmann, V., Weissmann, M., Cress, A., Filioglou, M., Komppula, M. and Reitebuch, O.: First Results from the German Cal/Val Activities for Aeolus, EPJ Web Conf. 237, 01008, doi:10.1051/epjconf/202023701008, 2020.

Bley, S., IT Consulting Group B.V., Aeolus Atmospheric Sampling − Range Bin Settings, available at https://www.aeolus.esa.int/confluence/pages/viewpage.action?spaceKey=CALVAL&title=Vs+002, 2021.

Boutle, I. A., Abel, S. J., Hill, P. G., Morcrette, C. J.: Spatial variability of liquid cloud and rain: observations and microphysical effects, Q. J. R. Meteorol. Soc., 140, 583–594, doi:10.1002/qj.2140, 2014.

Bucholtz, A.: Rayleigh-scattering calculations for the terrestrial atmosphere, Appl. Opt. 34, 2765−2773, 1995.

~~Chanin, M. L., Garnier, A., Hauchecorne, A. and Porteneuve, J.: A Doppler lidar for measuring winds in the middle atmosphere, Geophys. Res. Lett. 16(11), 1273–1276, doi:10.1029/GL016i011p01273, 1989.~~

Chahine, M. T., and 30 Coauthors: AIRS: Improving weather forecasting and providing new data on green-house gases, Bull. Amer. Meteor. Soc., 87(7), 911–926, doi:10.1175/BAMS-87-7-911, 2006.

Chalon G., Cayla F. R., Diebel D.: IASI: An advance sounder for operational meteorology, Proc. 52nd Congress of IAF, Toulouse France, CNES, available online at http://smsc.cnes.fr/documentation/IASI/Publications/PR ESENTATION_IAF_2001.pdf, 2001.

Chanin, M. L., Garnier, A., Hauchecorne, A. and Porteneuve, J.: A Doppler lidar for measuring winds in the middle atmosphere, Geophys. Res. Lett. 16(11), 1273–1276, doi:10.1029/GL016i011p01273, 1989.

Chepfer H., Bony, S., Winker, D., Chiriaco, M., Dufresne, J.-L., Sèze, G.: Use of CALIPSO lidar observations to evaluate the cloudiness simulated by a climate model, Geophys. Res. Let., 35, L15704, doi:10.1029/2008GL034207, 2008.

Chepfer H., Bony, S., Winker, D., Cesana,G., Dufresne, J.-L., Minnis, P., Stubenrauch, C. J., and Zeng, S.: The GCM Oriented Calipso Cloud Product (CALIPSO-GOCCP). J. Geophys. Res., 115, D00H16, doi:10.1029/2009JD012251, 2010.

Chepfer H., Cesana, G., Winker, D., Getzewich, B., Vaughan, M., and Liu, Z.: Comparison of two different cloud climatologies derived from CALIOP attenuated backscattered measurements (Level 1): the CALIPSO-ST and the CALIPSO-GOCCP. J. Atmos. Oceanic Technol., doi: 10.1175/JTECH-D-12-00057.1, 2012.

Chepfer H., Cesana, G., Winker, D., Getzewich, B., and Vaughan, M.: Comparison of two different cloud climatologies derived from CALIOP Level 1 observations: the CALIPSO-ST and the CALIPSO-GOCCP, J. Atmos. Ocean. Tech., , H., Noel30(4), 725−744 doi.10.1175/JTECH-D-12-00057.1, 2013.

Chepfer, H., Noël, V., Winker, D., and Chiriaco, M.: Where and when will we observe cloud changes due to climate warming?, Geophys. Res. Lett., 41, 8387–8395, doi:10.1002/2014GL061792, 2014.

Chepfer H., NoelNoël, V., Chiriaco, M., Wielicki, B., Winker, D., Loeb, N., and Wood, R.: The potential of multi-decades space-born lidar to constrain cloud feedbacks, J. Geophys. Res. Atmos., DOI:10.1002/2017JD027742, 2018.

Chepfer, H., Brogniez, H., and NoelNoël, V.: Diurnal variations of cloud and relative humidity profiles across the tropics, Sci. Rep., 9, 16045, doi:10.1038/s41598-019-52437-6, 2019.

Chiriaco, M., Vautard, R., Chepfer, H., Haeffelin, M., Dudhia, J., Wanherdrick, Y., Morille, Y., and A. Protat, A.: The Ability of MM5 to Simulate Ice Clouds: Systematic Comparison between Simulated and Measured Fluxes and Lidar/Radar Profiles at the SIRTA Atmospheric Observatory, Monthly Weather Rev., 134(3), 897−918, https://doi.org/10.1175/MWR3102.1, 2006.

Ciddor. P. E.: Refractive index of air: new equations for the visible and near infrared, Appl. Optics 35, 1566−1573, 1996.

Collis, R. T. H., Russell, P. B.: Lidar measurement of particles and gases by elastic backscattering and differential absorption, Laser Monitoring of the Atmosphere, Topics in Applied Physics, 14, ISBN 978-3-540-07743-5. Springer-Verlag, 71– 150, doi:10.1007/3-540-07743-X_18, 1976.

Dawkins, E. C. M., Feofilov, A., Rezac, L.,Kutepov, A. A., Janches, D., Höffner, J., X. Chu, X., Lu, X., Mlynczak, M. G, and Russell III, J.: Validation of SABER v2.0operational temperature data with ground-based lidars in the mesosphere-lower thermosphere region (75–105 km), J. Geophys. Res. Atmos., 123, 9916–9934, doi:10.1029/2018JD028742, 2018.

Donovan, D. P., Marseille, G.-J., de Kloe, J., and Stoffelen, A.: AEOLUS L2 activities at KNMI, EPJ Web Conf. 237, 01002, doi:10.1051/epjconf/20202370100, 2020.

Feofilov, A. G., Chepfer, H., NoelNoël, V., Guzman, R., Gindre, C., Ma, P.-L., and Chiriaco, M.: ColocatedCollocated ALADIN/Aeolus and CALIOP/CALIPSO observations for the period of 28/06/2019−31/12/2019, version 2, ResearchGate, https://doi.org/10.13140/RG.2.2.11237.12009 16562.94409, 2021.

Feofilov, A. G. and Petelina, S.V.: Relation between mesospheric ice clouds, temperature, and water vapor determined from Odin/OSIRIS and TIMED/SABER data, J.Feofilov, A. and Stubenrauch, C.: LMD Cloud Retrieval using IR sounders. Algorithm Theoretical Basis, CIRS-LMD software package V2, 19 pp., https://doi.org/10.13140/RG.2.2.15812.63361, 2017.

Geophys. Res, 115, D18305, doi:10.1029/ 2009JD013619, 2010.

Feofilov, A. G., Kutepov, A. A., She, C.-Y., Smith, A. K., Pesnell, W. D., and Goldberg, R. A.: CO2(v2)-O quenching rate coefficient derived from coincidental SABER/TIMED and Fort Collins lidar observations of the mesosphere and lower thermosphere, Atmos. Chem. Phys., 12, 9013–9023, doi:10.5194/acp-12-9013-2012, 2012.

Feofilov, A. G. and Stubenrauch, C. J.: Diurnal variation of high-level clouds from the synergy of AIRS and IASI space-borne infrared sounders, Atmos. Chem. Phys., 19, 13957–13972, doi:10.5194/acp-19-13957-2019, 2019.

Garnier, A., Pelon, J., Vaughan, M. A., Winker, D. M., Trepte, C. R., and Dubuisson, P.: Lidar multiple scattering factors inferred from CALIPSO lidar and IIR retrievals of semi-transparent cirrus cloud optical depths over oceans, Atmos. Meas. Tech., 8(7), 2759–2774, https://doi.org/10.5194/amt-8-2759-2015, 2015.

Guzman, R., Chepfer, H., ~~Noel~~Noël, V., Vaillant de Guelis, T., Kay, J. E., Raberanto, P., Cesana, G., Vaughan, M. A., and Winker, D. M.: Direct atmosphere opacity observations from CALIPSO provide new constraints on cloud-radiation interactions, J. Geophys. Res. Atmos., 122, 1066–1085, doi:10.1002/2016JD025946, 2017.

~~Héliere, A., Gelsthorpe, R., Le Hors, L., and Toulemont, Y.: ATLID, the Atmospheric Lidar on board the EarthCARE Satellite, Proceedings of the ICSO (International Conference on Space Optics), Ajaccio, Corse, France, Oct. 9-12, 2012, paper: ICSO-065, 2012.~~

~~Hilton, F., and 42 Coauthors, Hyperspectral Earth observation from IASI: Five years of accomplishments, Bull. Am. Meteorol. Soc., 93, 347–370, doi:10.1175/BAMS-D-11-00027.1, 2012.~~

Flamant, P., Cuesta, J., Denneulin, M.-L., Dabas, A., and Hubert, D.: ADM-Aeolus retrieval algorithms for aerosol and cloud products, Tellus, 60(2), 273-288, doi:10.1111/j.1600-0870.2007.00287.x. 2008.

Flamant, P. H., Lever, V., Martinet, P., Flament, T., Cuesta, J., Dabas, A., Olivier, M., and Huber, D.: ADM-Aeolus L2A Algorithm Theoretical Baseline DocumentParticle spin-off products, AE-TN-IPSL-GS-001, V5.5, ESA, available online at https://earth.esa.int/eogateway/documents/20142/0/Aeolus-L2A-Algorithm-Theoretical-Baseline-Document.pdf, 83pp, 2017.

~~Holl, G., Buehler, S. A., Rydberg, B., and Jiménez, C.: Collocating satellite-based radar and radiometer measurements – methodology and usage examples, Atmos. Meas. Tech., 3, 693–708, doi:10.5194/amt-3-693-2010, 2010.~~

Héliere, A., Gelsthorpe, R., Le Hors, L., and Toulemont, Y.: ATLID, the Atmospheric Lidar on board the EarthCARE Satellite, Proceedings of the ICSO (International Conference on Space Optics), Ajaccio, Corse, France, Oct. 9-12, 2012, paper: ICSO-065, 2012.

Hilton, F., and 42 Coauthors, Hyperspectral Earth observation from IASI: Five years of accomplishments, Bull. Am. Meteorol. Soc., 93, 347– 370, doi:10.1175/BAMS-D-11-00027.1, 2012.

Jumelet, J., Bekki, S., David, C., Keckhut, P., Baumgarten, G.: Size distribution time series of a polar stratospheric cloud observed above Arctic Lidar Observatory for Middle Atmosphere Research (ALOMAR) (69°N) and analyzed from multiwavelength lidar measurements during winter 2005, J. Geophys. Res., 114(D02202), doi:10.1029/2008JD010119, 2019.

Kanitz, T., and 24 Coauthors, ESA's Lidar Missions Aeolus and EarthCARE, EPJ Web Conf. 237, 01006, doi:10.1051/epjconf/202023701006, 2020.

Krawczyk, R., Ghibaudo, J.-B., Labandibar, J.-Y., Willetts, D. V., Vaughan, M., Pearson, G. N., Harris, M. R., Flamant, P. H., Salamitou, P., Dabas, A. M., Charasse, R., Midavaine, T., Royer, M., and Heimel, H.: ALADIN: an atmosphere laser Doppler wind lidar instrument for wind velocity measurements from space, Proc. SPIE 2581, Lidar Techniques for Remote Sensing II, (15 December 1995); doi:10.1117/12.228509, 1995.

Lolli, S., Delaval, A., Loth, C., Garnier, A., and Flamant, P. H.: 0.355-micrometer direct detection wind lidar under testing during a field campaign in consideration of ESA's ADM-Aeolus mission, Atmos. Meas. Tech., 6, 3349–3358, doi:10.5194/amt-6-3349-2013, 2013.

Nam C., Bony, S., Dufresne, J.L., Chepfer, H.: The 'too few, too bright' tropical low-cloud problem in CMIP5 models, Geophys. Res. Lett., 39, 21, doi:10.1029/2012GL053421, 2012.

Noël, V., Hertzog, A., Chepfer, H., Winker, D.: Polar stratospheric clouds over Antarctica from the CALIPSO space-borne lidar, J. Geophys. ~~Noel~~Res. Atm., 113(D2), D02205, https://doi.org/10.1029/2007JD008616, 2008.

Noël, V., Chepfer, H., Chiriaco, M., and Yorks, J.: The diurnal cycle of cloud profiles over land and ocean between 51∘ S and 51∘ N, seen by the CATS ~~spaceborne~~space-borne lidar from the International Space Station, Atmos. Chem. Phys., 18, 9457–9473, doi:10.5194/acp-18-9457-2018, 2018.

McGill, M. J., Yorks, J. E., Scott, V. S., Kupchock, A. W., and Selmer, P. A.: The Cloud-Aerosol Transport System (CATS): A technology demonstration on the International Space Station, Proc. Spie., 9612, doi:10.1117/12.2190841, 2015.

Menzel, W. P., Frey, R. A., Borbas, E. E., Baum, B. A., Cureton, G., and Bearson, N.: Reprocessing of HIRS Satellite Measurements from 1980 to 2015: Development towards a consistent decadal cloud record, J. Appl. Meteorol. Clim., 55, 2397–2410, doi:10.1175/JAMC-D-16-0129.1, 2016.

Rasch, P., and 41 Coauthors: An Overview of the Atmospheric Component of the Energy Exascale Earth System Model, J. Adv. Model. Earth Syst., jame20932, doi:10.1029/2019MS001629, 2019.

Reitebuch, O., and 27 Coauthors: Initial Assessment of the Performance of the First Wind Lidar in Space on Aeolus, EPJ Web Conf. 237, 01010, doi:10.1051/epjconf/202023701010, 2020.

Reverdy M., Chepfer, H., Donovan, D., ~~Noel~~Noël, V., Cesana, G., Hoareau, C., Chiriaco, M., Bastin, S.: An EarthCARE/ATLID simulator to evaluate cloud description in climate models, J. Geophys. Res. Atmos., 120(21), 11090−11113, doi: 10.1002/2015JD023919, 2015.

Rienecker, M.: File Specification for GEOS-5 DAS Gridded Output, Document No. GMAO-1001v6.4, NASA Goddard Space Flight Center, available online at https://gmao.gsfc.nasa.gov/GMAO_products/documents/GEOS-5.2.0_File_Specification.pdf, 2008.

Smith, W. L.: The TIROS-N operational vertical sounder, Bull. Am. Meteorol. Soc., 60, 1177–1187, 1979.

Snels, M., Colao, F., Cairo, F., Shuli, I., Scoccione, A., De Muro, M., Pitts, M., Poole, L., and Di Liberto, L.: Quasi-coincident observations of polar stratospheric clouds by ground-based lidar and CALIOP at Concordia (Dome C, Antarctica) from 2014 to 2018, Atmos. Chem. Phys., 21, 2165–2178, doi:10.5194/acp-21-2165-2021, 2021.

Stephens, G. L., Vane, D. G., ~~Hakuba~~Tanelli, S., Im, E., Durden, S., Rokey, M. ~~Z., Webb, M.~~., Reinke, D., Partain, P., Mace, G. G., Austin, R., L'Ecuyer, T., Haynes, J., Lebsock, M., ~~Yue,Q., Kahn, B. H., Hristova-Veleva, S., Rapp, A. D., Stubenrauch, C.~~Suzuki, K., Waliser, D., Wu, D., Kay, J., ~~Elsaesser, G. S~~Gettelman, A., Wang, Z., and ~~Slingo, J.: Regional Intensification of~~ Marchand, R.: CloudSat mission: Performance and early science after the ~~Tropical Hydro-logical Cycle~~

During ENSO,first year of operation, J. Geophys. Res. Lett., 45, 4361 4370, doi :Atm., 114, D00A18, DOI: 10.1029/2018GL077598, 20182008Jd009982, 2009.

Stoffelen, A., Pailleux, J., Källén, E., Vaughan, J. M., Isaksen, L., Flamant, P., Wergen, W., Andersson, E., Schyberg, H., Culoma, A., Meynart, R., Endemann, M., and Ingmann, P.: The Atmospheric Dynamics Mission For Global Wind Field Measurement, Bull. Amer. Meteor. Soc., 86, 73–87, doi: 10.1175/BAMS-86-1-73, 2005.

Straume, A. G., and 27 Coauthors: ESA's Space-Based Doppler Wind Lidar Mission Aeolus – First Wind and Aerosol Product Assessment Results, EPJ Web Conf. 237, 01007, doi:10.1051/epjconf/20202370100, 2020.

Stubenrauch, C. J., and 22 Coauthors: Assessment of global cloud datasets from satellites: Project and database initiated by the GEWEX radiation panel, Bull. Am. Meteorol. Soc., 94(7), 1031–1049, doi:10.1175/BAMS-D-12-00117.1, 2013.

Stubenrauch, C. J., Feofilov, A. G., Protopapadaki, S. E., and Armante, R.: Cloud climatologies from the infrared sounders AIRS and IASI: strengths and applications, Atmos. Chem. Phys., 17, 13625–13644, doi:10.5194/acp-17-13625-2017, 2017.

Swales, D. J., Pincus, R., & Bodas-Salcedo, A.: The cloud feedback model intercomparison project observational simulator package: Version 2. Geoscientific Model Development, 11, 77– 81, doi:10.5194/gmd-11-77-2018, 2018.

Vaillant de Guélis T., H. Chepfer, NoelNoël, V., Guzman, R., Bonazzola, M., and Winker, D. M.: Space lidar observations constrain longwave cloud feedback, Nature Sci. Rep., 8:16570, doi:10.1038/s41598-018-34943-1, 2018.

Virtanen, T. H., Kolmonen, P., Sogacheva, L., Rodríguez, E., Saponaro, G., and de Leeuw, G.: Collocation mismatch uncertainties in satellite aerosol retrieval validation, Atmos. Meas. Tech., 11, 925–938, doi:10.5194/amt-11-925-2018, 2018.

Weiler, F., Kanitz, T., Wernham, D., Rennie, M., Huber, D., Schillinger, M., Saint-Pe, O., Bell, R., Parrinello, T., and Reitebuch, O.: Characterization of dark current signal measurements of the ACCDs used on-board the Aeolus satellite, Atmos. Meas. Tech. Discuss. [preprint], ., 14, 5153–5177, https://doi:.org/10.5194/amt-2020-458, in review, 202014-5153-2021, 2021.

Winker, D. M.: Accounting for multiple scattering in retrievals from space lidar, Proc. SPIE Int. Soc. Opt. Eng., 5059, 128–139, 2003.

Winker, D. M., Hunt, W. H., and Hostetler, C. A.: Status and Performance of the CALIOP Lidar, Proc. SPIE vol 5575, 8-15, 2004.

Winker, D. M., Hunt, W. H., and McGill, M. J.: Initial performance assessment of CALIOP, Geophys. Res. Lett., 34, L19803, doi:10.1029/2007GL030135, 2007.

Winker, D. M., Vaughan, M. A., Omar, A. H., Hu, Y., Powell, K. A., Liu, Z., Hunt, W. H., and Young, S. A.: Overview of the CALIPSO Mission and CALIOP Data Processing Algorithms, J. Atmos. Ocean. Tech., 26, 2310–2323, doi:10.1175/2009JTECHA1281.1, 2009.

Winker, D., Chepfer, H., Noël, V., and Cai, X.: Observational constraints on cloud feedbacks: The role of active satellite sensors. Surveys in Geophysics, 38, 1483−1508, https://doi.org/10.1007/s10712-017-9452-0, 2017.

Mis en forme : Anglais (États-Unis)

Zelinka, M. D., Myers, T. A., McCoy, D. T., Po-Chedley, S., Caldwell, P. M., Ceppi, P., Klein, S. A., Taylor, K. E.: Causes of Higher Climate Sensitivity in CMIP6 Models, Geophys. Res. Lett, 47(1), e2019GL085782, https://doi.org/10.1029/2019GL085782, 2020.

Instrument	Orbit inclination [deg]	Equator crossing LT [h]	Off-nadir angle [deg]	PRF [Hz]	Native resolution [m]	L2 resolution resolution [m]
ALADIN	96.97	6:00 / 18:00	35	50.0	140 (H) x 1000250-2000 (V)	87000 (H) x 1000250-2000 (V)
CALIOP	98.00	01:30 / 13:30	3	20.1	333 (H) x 60 (V)	333 (H) x 500(V)

Table 1: Comparison of orbital parameters, viewing geometries, and resolutions of ALADIN and CALIOP instruments

Δtime [h]	Daytime ×1E3	Night-time ×1E3	Total ×1E3	Remarks
< 1	4.31	3.74	87.5	Narrow polar zone
< 34	13.125	11.250	24.375	Broader polar zone
< 6	9190	7877	169167	All zones covered
< 9	120	108	228	
< 12	135133	116115	251248	Unequal distribution of Δtime
< 24	176173	146144	322317	Unequal distribution of Δtime

Table 2: Number of collocated cases for Δdist < 1° and different Δtime values

Mis en forme : Centré
Tableau mis en forme
Cellules supprimées
Tableau mis en forme
Tableau mis en forme
Cellules supprimées

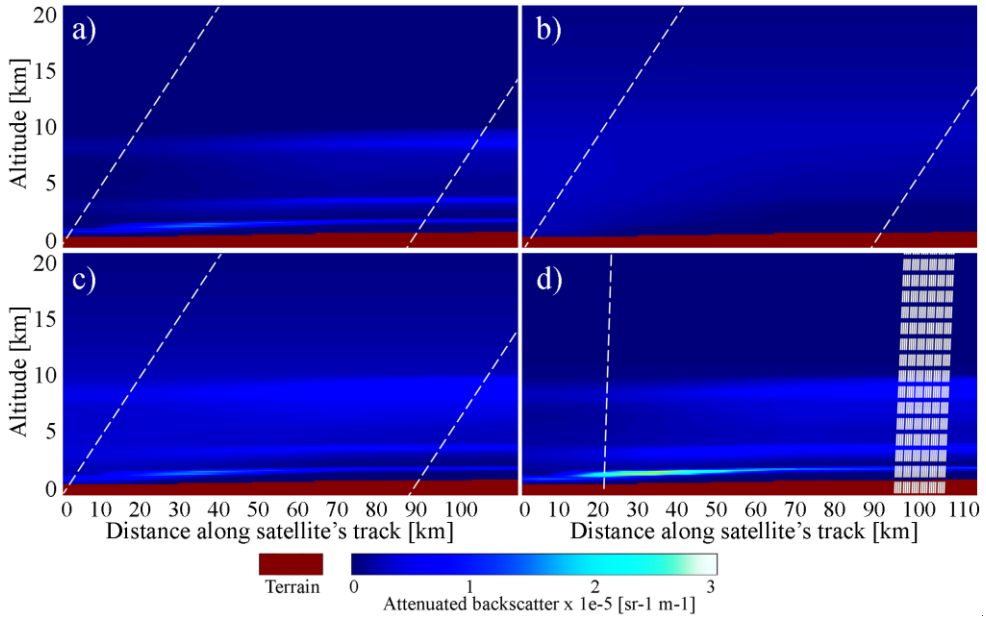

~~Figure 1: Observation geometry, averaging, and retrieved parameters for (a-c) ALADIN/Aeolus at its L2A resolution of 87 km and (d) CALIOP/CALIPSO at its native resolution: (a) Attenuated particular backscatter (APB) at 355 nm; (b) Attenuated molecular backscatter (AMB) at 355 nm; (c) Attenuated total backscatter (ATB) at 355 nm; (d) Attenuated total backscatter (ATB) at 532 nm. The scene has been calculated for demonstration purposes using COSP2 simulations with the EAMV1 model data as an input. White dashed lines stand in (a-c) for ALADIN's observation paths for centers of averaged profiles and in (d) for CALIOP averaged observation path corresponding to averaged ALADIN on the left and for individual CALIOP profiles on the right (with its 3° off-nadir viewing angle). ALADIN observes the atmosphere at 35° to the nadir and perpendicular to the flight direction. This inclination is schematically shown as an inclined line lying in lidar curtain plane whereas the real projection to the same plane should be a vertical line.~~

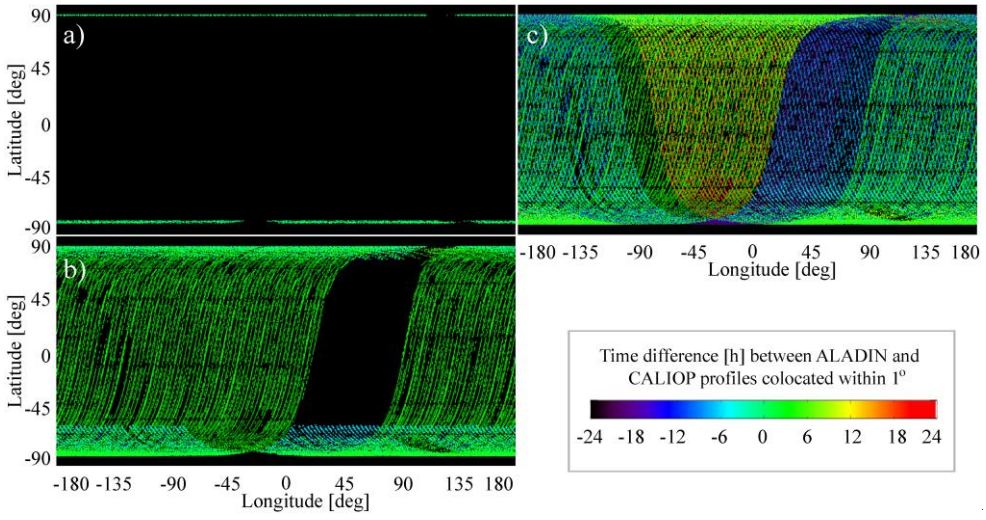

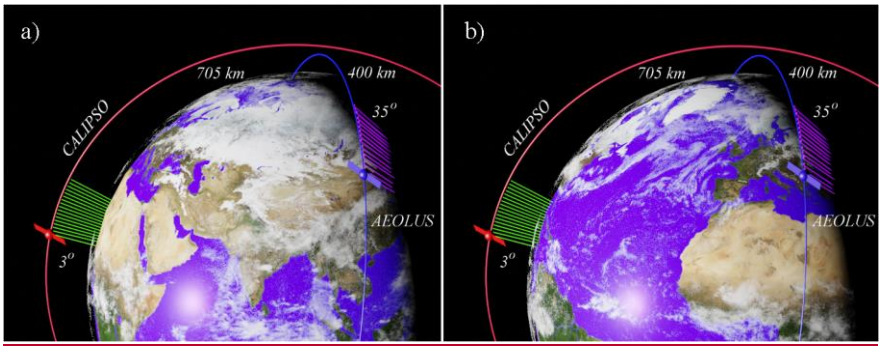

Figure 1: Observation geometry and orbits of ALADIN/Aeolus and CALIOP/CALIPSO space borne lidars. ALADIN observes the atmosphere at dawn-dusk, whereas CALIOP passes the equator at 01:30 and 13:30 local solar time. The difference between (a) and (b) panels is in the position of Earth and the time: in (b), AEOLUS overflies the same area (centered over Africa) as was observed by CALIOP ~4.5 h earlier (in (a)).

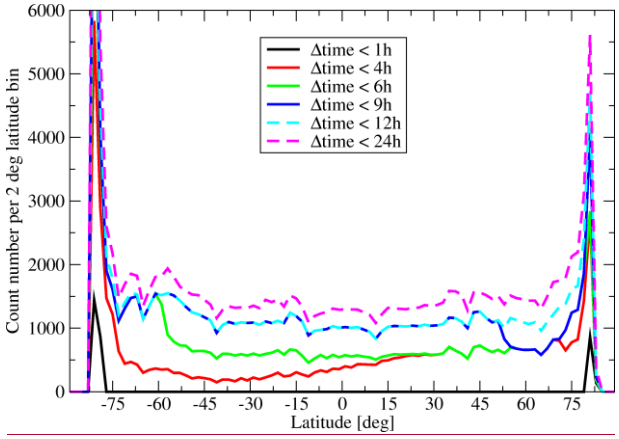

Figure 2: ~~**Geographical distribution**~~**Latitudinal coverage** **of collocated points for** ~~**(a)**~~ **Δdist < 1° and different limits for Δtime < 1 h**~~**; (b) Δtime < 6 h; (c) Δtime < 24 h for Δdist < 1°.**~~**.**

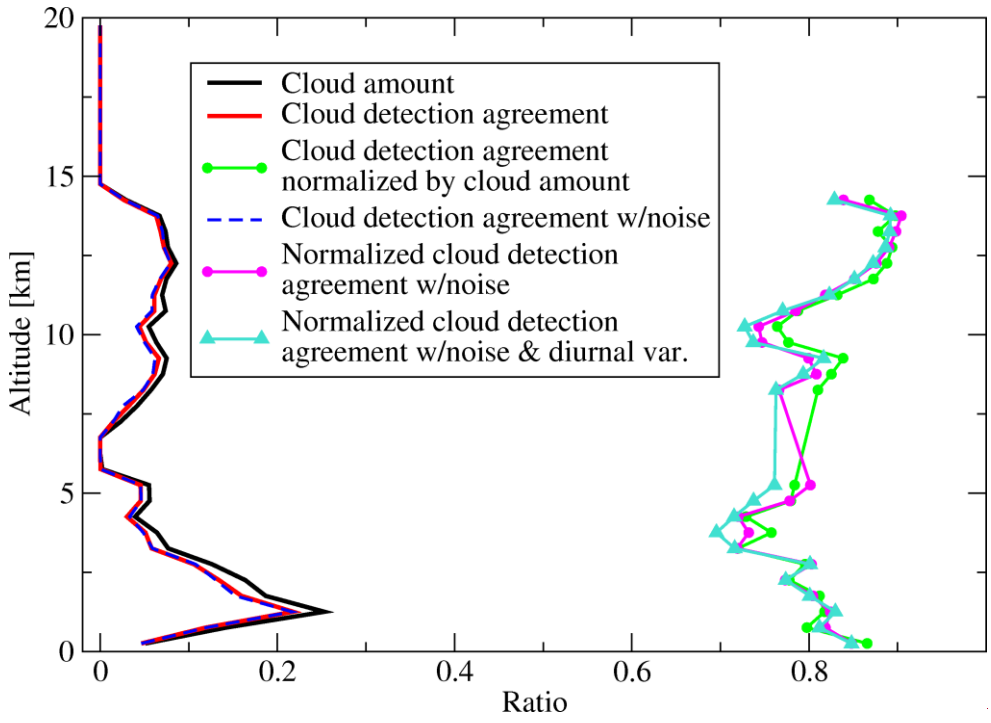
Cloud amount
Cloud detection agreement
Cloud detection agreement normalized by cloud amount
Cloud detection agreement w/noise
Normalized cloud detection agreement w/noise
Normalized cloud detection agreement w/noise & diurnal var.
Altitude [km]
Ratio
0
5
10
15
20
0
0.2
0.4
0.6
0.8

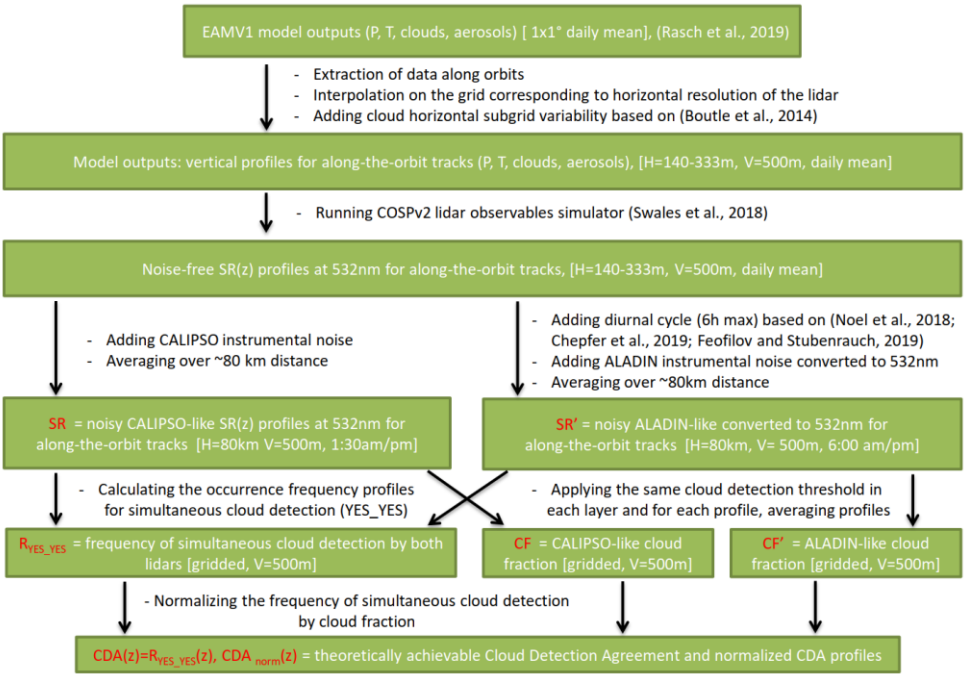

Figure 3: A flowchart explaining the numerical experiment on estimating the best possible cloud detection agreement for a combination of ALADIN and CALIOP observations. Green boxes list the input and output data. Black text between boxes describes actions performed on each dataset. Red text in the boxes marks the datasets used in the estimation. White text in square brackets in the boxes indicates horizontal (H) and vertical (V) resolutions of the datasets.

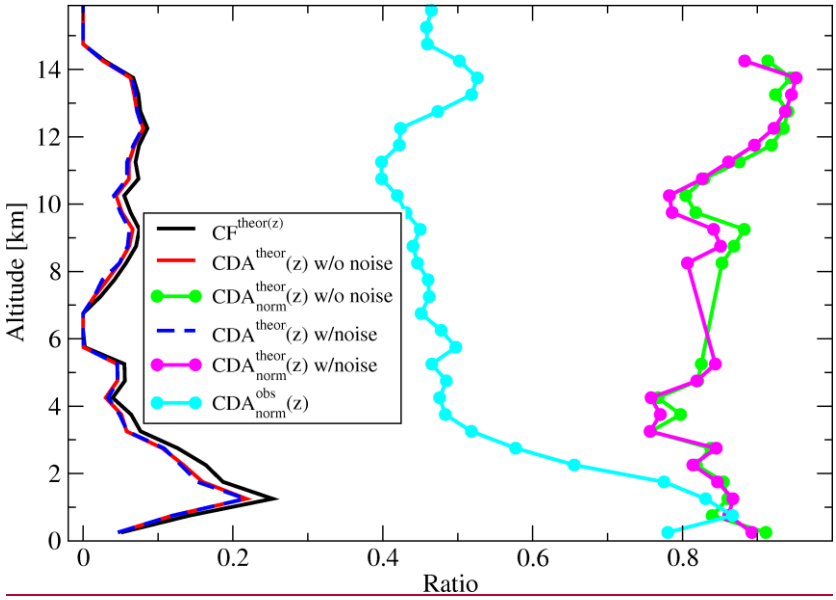

**Figure 4: Estimating theoretical cloud detection agreement using pseudo-collocated ~~scattering ratio (SR) data~~ $SR(532nm, z)$ and $SR'(532nm, z)$ profiles calculated using COSP2 lidar simulator coupled with the output of the EAMv1 atmospheric model~~. For each altitude bin, the agreement is defined as a ratio of number of cases when both CALIOP and ALADIN have detected a cloud to a total number of simulations for a~~ (see Fig. 3). The definitions of CF(z), CDA(z), and CDA_{norm}(z) variables are given ~~bin. The cloud amount corresponds to a ratio of number of cases when a reference CALIOP SR value without~~in Section 3.5. "Noise" stands for calculations considering experimental noise ~~was above the detection threshold to a total number of simulations for a given bin.~~of CALIOP and ALADIN and diurnal variation of the clouds for the collocation Δtime up to 6 h (see Fig. 2). The ~~normalized cloud detection agreement represents a ratio of the former to the latter.~~"$CDA_{norm}^{obs}(z)$" cyan curve comes from the analysis of real collocated data and is mentioned in Section 5.3.

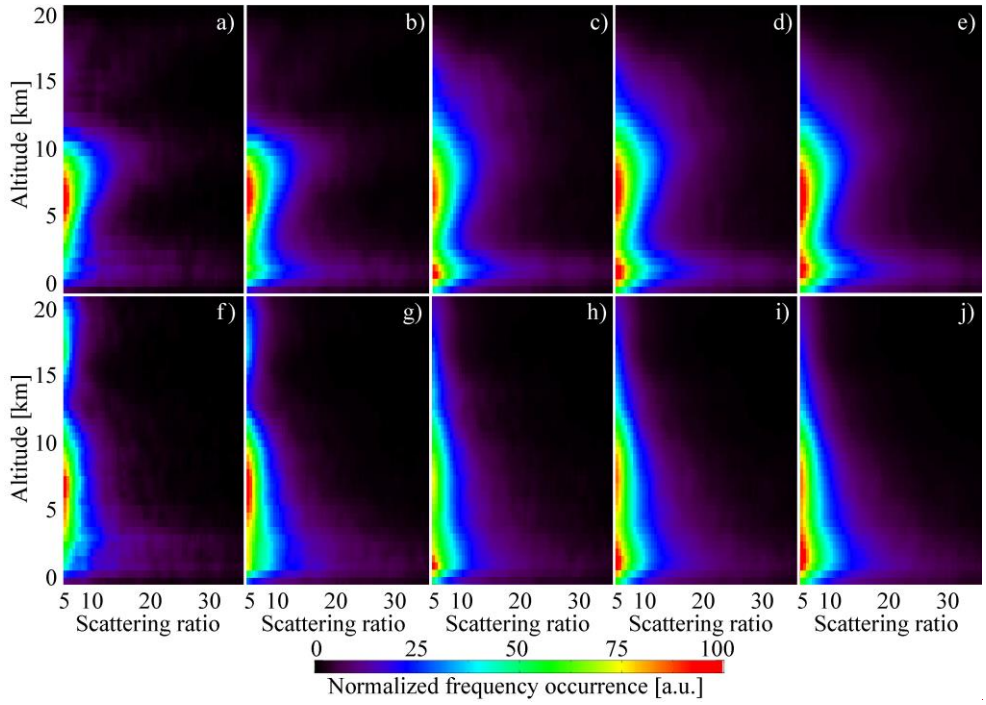
a)
b)
c)
d)
e)
f)
g)
h)
i)
j)
Altitude [km]
20
15
10
5
0
5 10 20 30
Scattering ratio
0 25 50 75 100
Normalized frequency occurrence [a.u.]

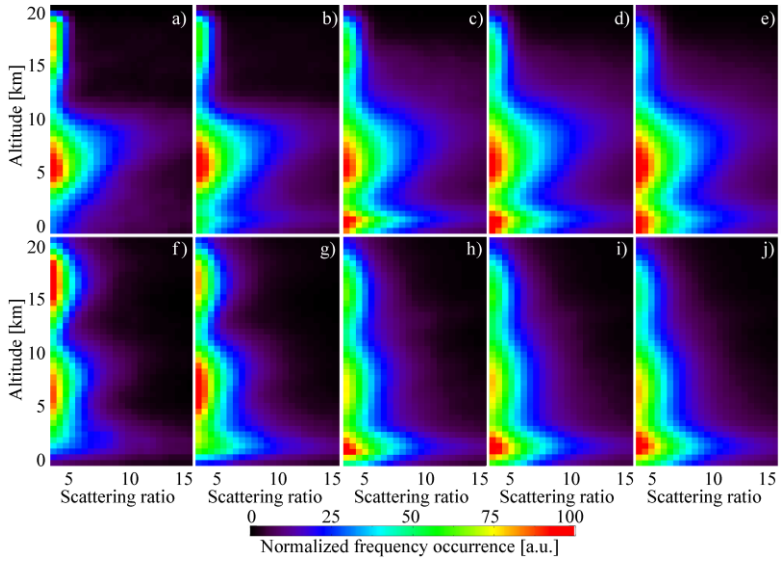

Figure 45: Zonal mean ~~comparison~~SR-height distributions for the Δtime < 6h, Δdist < 1° collocated nighttime data subset (see Table 2): (a)-(e) CALIOP $SR(532nm, z)$ averages; (f)-(j) $SR'(532nm, z)$ estimated from ALADIN ~~averages, converted to SR at 532 nm for comparison purposes~~extinction and backscatter coefficients; (a,f) 90S-60S; (b,g) 60S-30S; (c,h) 30S-30N; (d,i) 30N-60N; (e,j) 60N-90N.

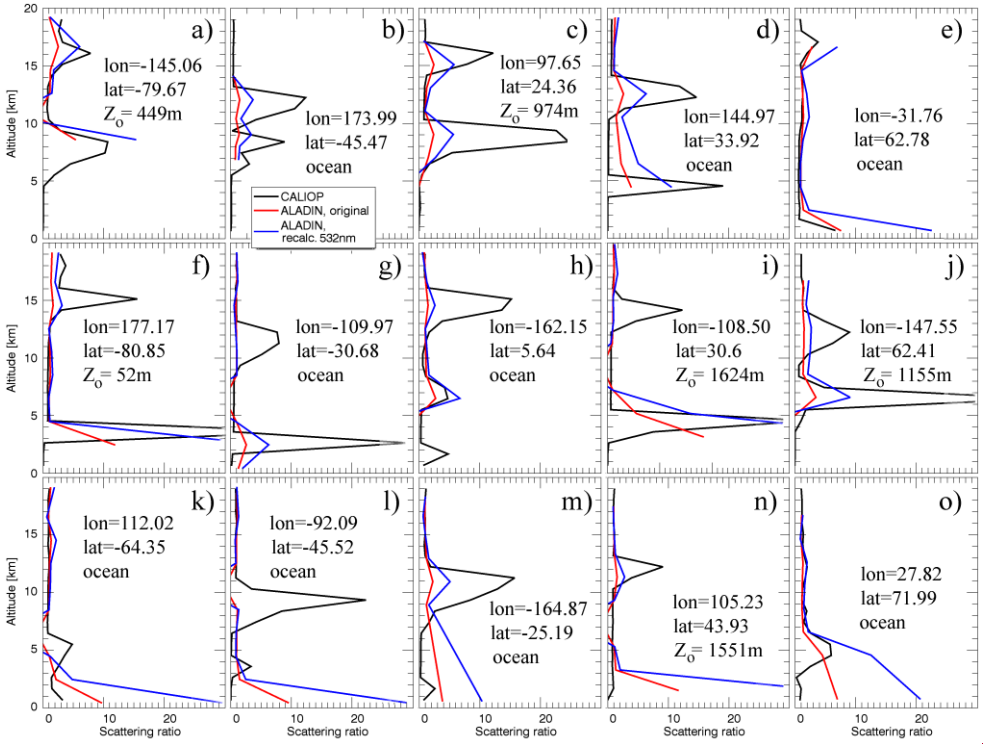
a)
lon=-145.06
lat=-79.67
Z$_o$= 449m
b)
lon=173.99
lat=-45.47
ocean
CALIOP
ALADIN, original
ALADIN, recalc. 532nm
c)
lon=97.65
lat=24.36
Z$_o$= 974m
d)
lon=144.97
lat=33.92
ocean
e)
lon=-31.76
lat=62.78
ocean
f)
lon=177.17
lat=-80.85
Z$_o$= 52m
g)
lon=-109.97
lat=-30.68
ocean
h)
lon=-162.15
lat=5.64
ocean
i)
lon=-108.50
lat=30.6
Z$_o$= 1624m
j)
lon=-147.55
lat=62.41
Z$_o$= 1155m
k)
lon=112.02
lat=-64.35
ocean
l)
lon=-92.09
lat=-45.52
ocean
m)
lon=-164.87
lat=-25.19
ocean
n)
lon=105.23
lat=43.93
Z$_o$= 1551m
o)
lon=27.82
lat=71.99
ocean
Altitude [km]
Scattering ratio

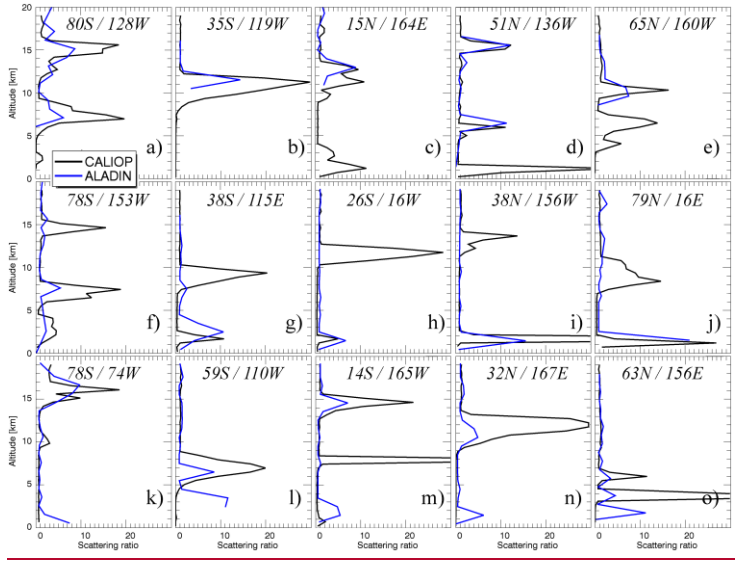

Figure 56: Pseudo-instantaneous comparisons of collocated ALADIN L2A SR profiles and CALIOP SR profiles averaged over 67 km along the track: (a, f, k) 90S-60S; (b, g, l) 60S-30S; (c, h, m) 30S-30N; (d, i , n) 30N-60N; (e, j, o) 60N-90N; (a-e) cases confirming ALADIN's capability to detect high-level clouds; (f-j) cases showing the cases when ALADIN misses a high cloud detected by CALIOP; (k-no) cases explaining the presumably false detection of a showing a low level cloud detected by ALADIN; (o) a case with a real low and not detected bu CALIOP in the presence of a higher thick cloud detected by both instruments with an extra point near the surface reported by ALADIN.

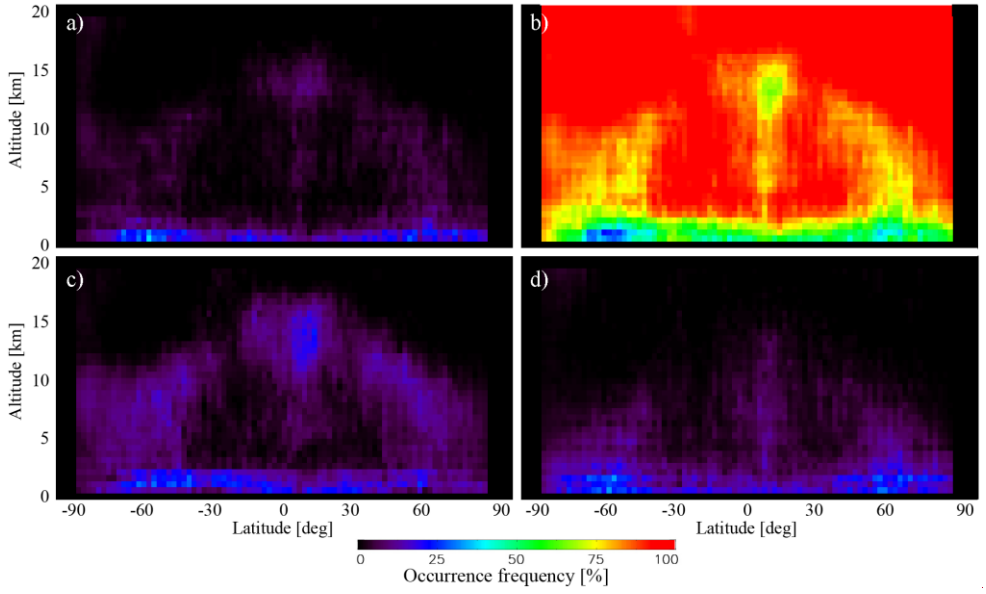
a)
b)
c)
d)
Altitude [km]
20
15
10
5
0
-90
-60
-30
0
30
60
90
Latitude [deg]
0
25
50
75
100
Occurrence frequency [%]

1000

~~Figure 6: Cloud detection agreement~~

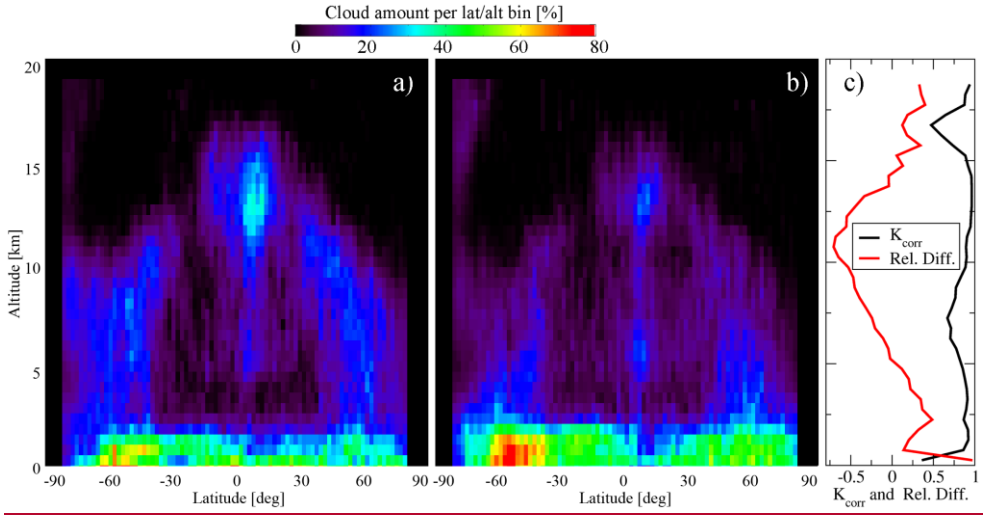

Figure 7: Latitudinal/altitudinal distributions of cloud amount defined from (a) CALIOP and (b) ALADIN, and altitudinal profiles of Pearson's correlation coefficient and relative difference between ALADIN and CALIOP (c).

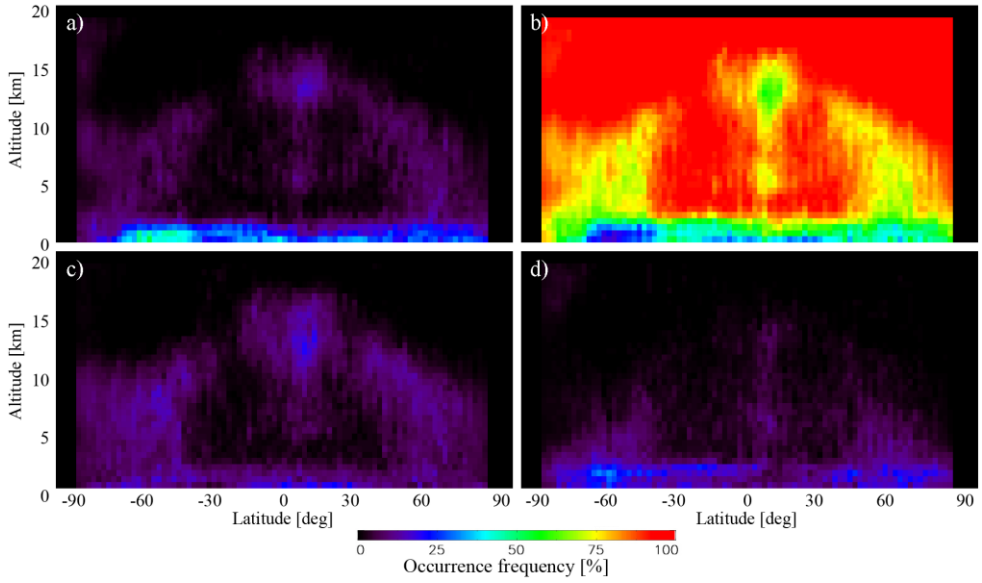

Figure 8: Occurrence frequency for collocated observations: a) both CALIOP and ALADIN ~~have~~ detected a cloud (~~YES/YES cases); b)~~ $R_{YES\_YES}(lat, z)$; b)** neither CALIOP nor ALADIN ~~has~~ detected a cloud (~~NO/NO cases);~~ $R_{NO\_NO}(lat, z)$**; c) CALIOP ~~has detected a cloud whereas ALADIN has not~~ detected a cloud ~~YES/NO cases);~~, whereas ALADIN missed a cloud (**$R_{YES\_NO}(lat, z)$**; d) CALIOP ~~does not detect~~missed a cloud, whereas ALADIN ~~has~~ detected a cloud (~~NO/YES cases).~~** $R_{NO\_YES}(lat, z)$**.**

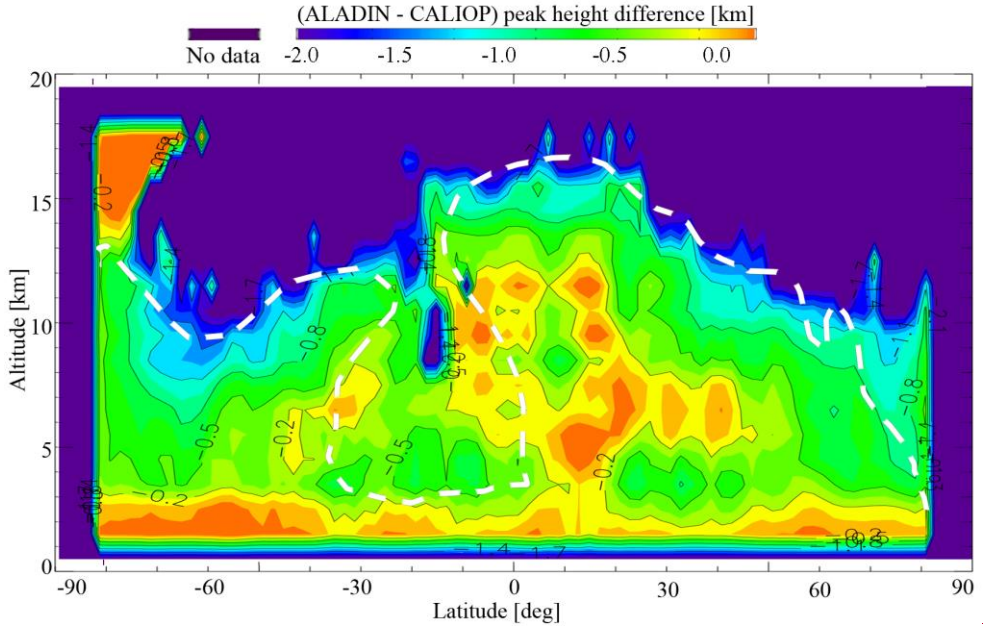
(ALADIN - CALIOP) peak height difference [km]
No data
-2.0
-1.5
-1.0
-0.5
0.0
Altitude [km]
Latitude [deg]
20
15
10
5
0
-90
-60
-30
0
30
60
90

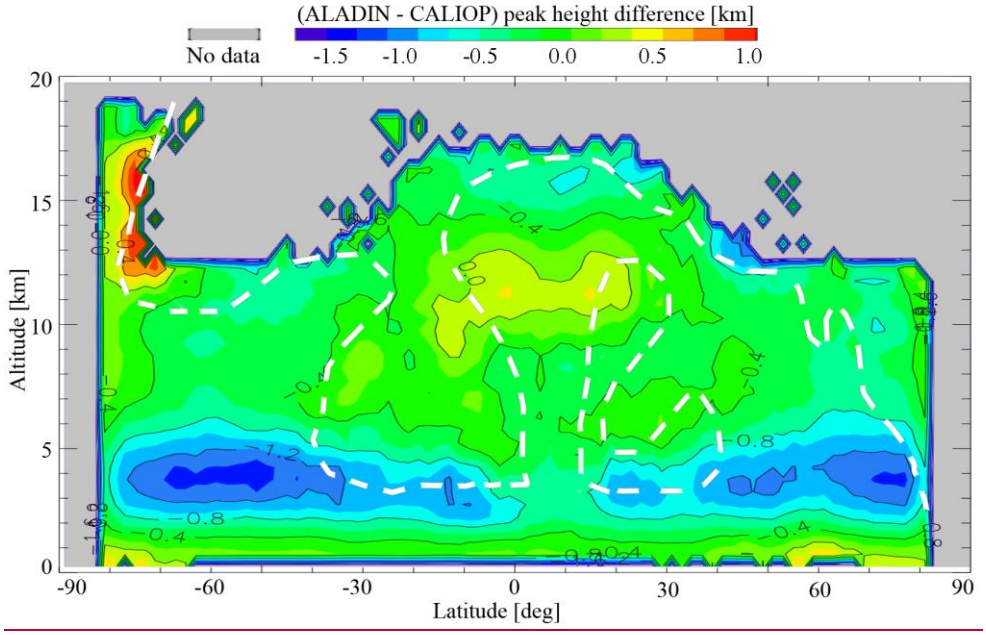

Figure ~~7~~9: Cloud altitude detection sensitivity represented as a height difference between the CALIOP local peak height and corresponding ALADIN's cloud peak height or maximal SR height found in the ±3 km vertical vicinity of CALIPSO peak. The subset corresponding to YES_YES selection (Fig. ~~6a~~8a) was used. White dashed isoline corresponds to colored area in Fig. ~~6a~~8a (occurrence frequency of about 5% and higher).

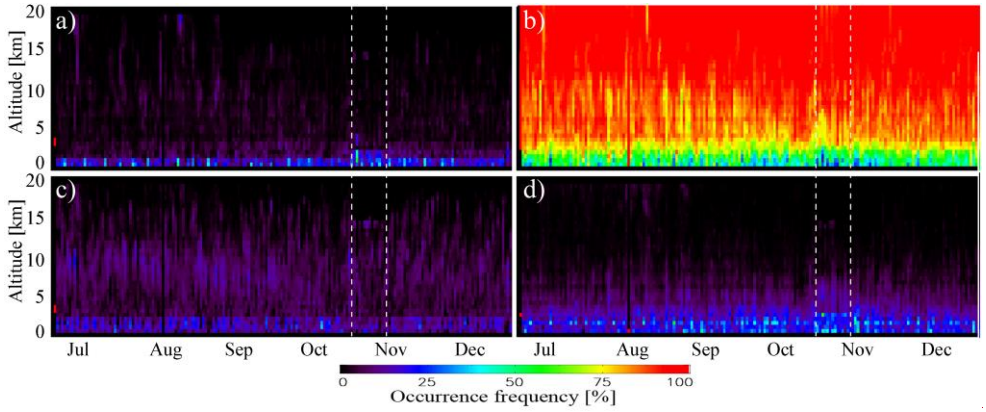

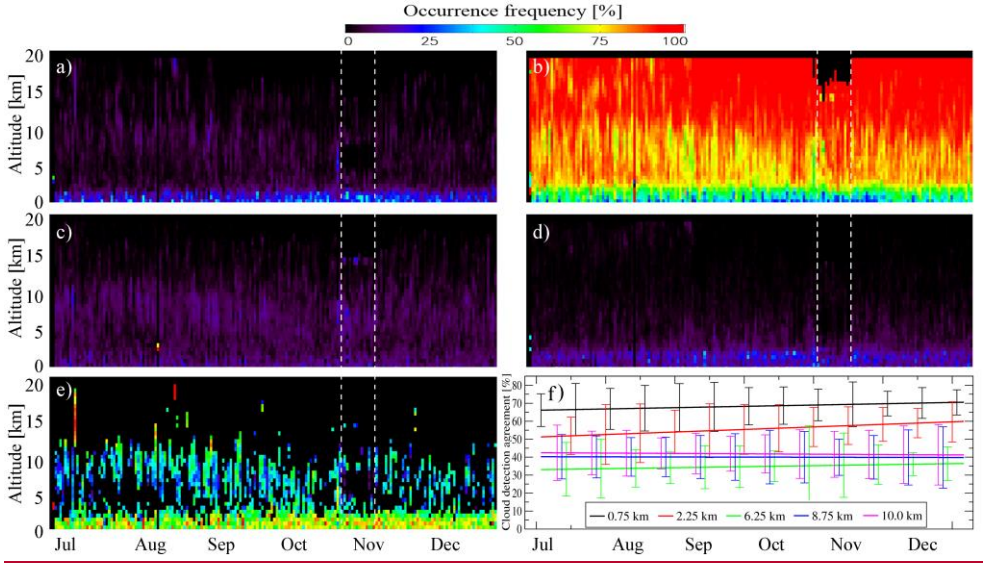

Figure ~~8~~10: Temporal evolution of ~~cloud detection agreement~~occurrence frequencies for a) $R_{YES\_YES}(z, time)$; b) $R_{NO\_NO}(z, time)$; c) $R_{YES\_NO}(z, time)$; d) $R_{NO\_YES}(z, time)$ for the period of 28/06/2019-31/12/2019. The legend is consistent with that of Fig. ~~6: a) YES/YES; b) NO/NO; c) YES/NO; d) NO/YES.~~ 8. White vertical dashed lines correspond to the ~~period of~~ Air Motion Vector (AMV) campaign (28/10/2019−10/11/2019), which is characterized by smaller bin sizes and, therefore, larger SNRs for Mie and Rayleigh channels up to the height of 2250m~~.~~

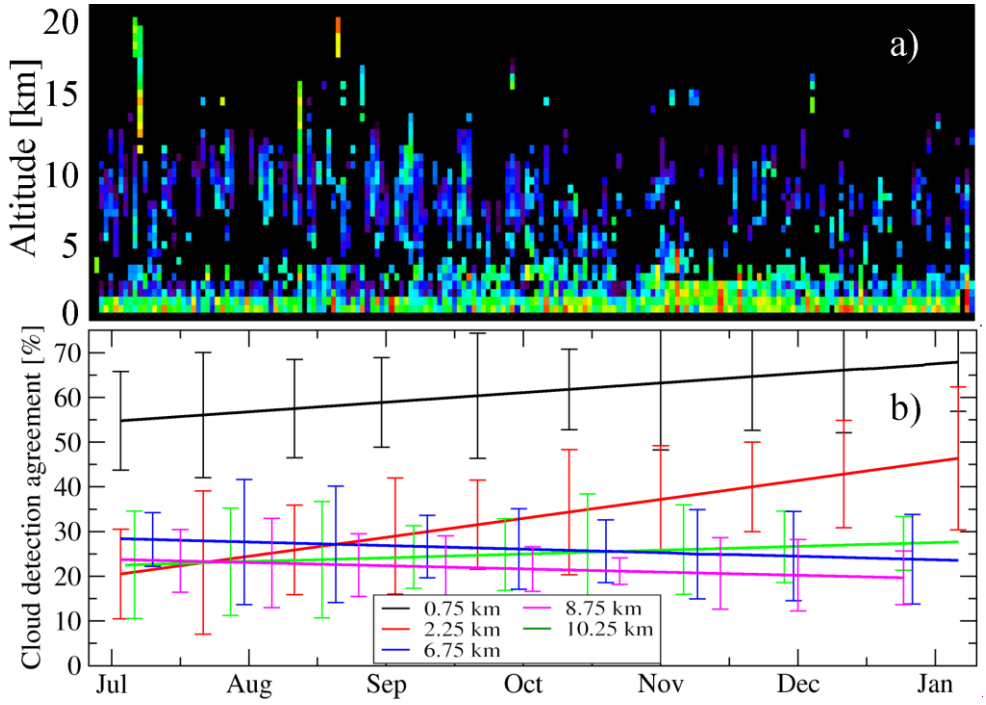

~~Figure 9: Temporal evolution of~~ ; e) normalized cloud detection agreement ~~for the period of 28/06/2019-31/12/2019: a) YES_YES statistics of Fig. 8a normalized by cloud amount; b) the~~ $CDA_{norm}(z, time)$; f) same ~~information~~as (e) presented for 5 heights as linear fits in 2D with error bars. ~~The color scheme for panel (a) is consistent with that of Fig. 8.~~

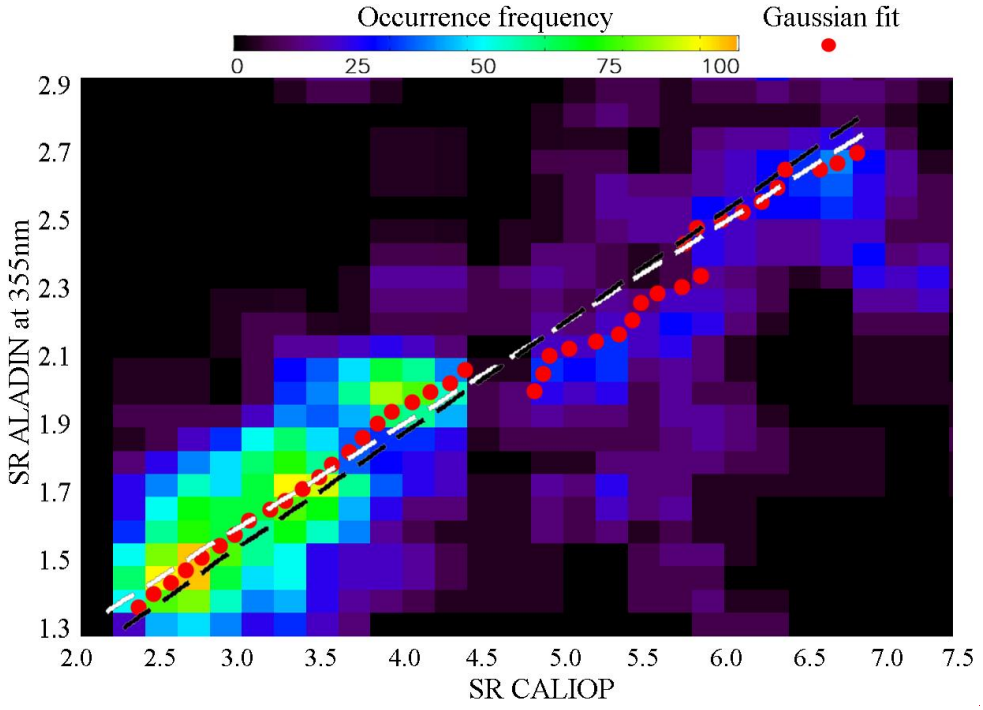

~~Figure A1: Correlation between individual pairs of CALIOP and ALADIN scattering ratio profiles, for all altitudes. The colors of the bins represent the occurrence frequencies for 0.2 × 0.07 SR bins, as a function of both CALIOP's SR_{532} and ALADIN's SR_{355}. For each point along the diagonal, a Gaussian was fitted to the data points lying along a perpendicular transect and the central point of the Gaussian is plotted~~The error bars were estimated as ~~a red filled circle. The white dashed line represents a linear fit to these points. For comparison, black dashed line shows the fit given by Eq.~~ root-mean-square values for 1~~.~~

-week chunks of altitude subsets.

Mis en forme : Légende